Search for QCD-Instanton-induced Processes in Deep Inelastic Scattering at HERA

Dissertation
zur Erlangung des Doktorgrades
des Fachbereichs Physik
der Universität Hamburg

vorgelegt von
Michael Sievers
aus Hamburg

Hamburg
2000

Gutachter der Dissertation:	Prof. Dr. E. Lohrmann Prof. Dr. R. Felst
Gutachter der Disputation:	Prof. Dr. E. Lohrmann Prof. Dr. R. Heinzelmann
Datum der Disputation:	24.07.2000
Dekan des Fachbereichs Physik und Vorsitzender des Promotionsausschusses:	Prof. Dr. F.-W. Büßer

Zusammenfassung

Eine Grenze des QCD-Instanton-induzierten Wirkungsquerschnitts wurde an Hand der im Jahre 1997 durch den ZEUS-Detektor aufgezeichneten Daten, insgesamt 26pb^{-1}, bestimmt. Dabei wurden Ereignisse der tiefunelastischen Streuung im Bereich $Q^2 > 75\text{GeV}^2$ und $x > 10^{-3}$ untersucht.

Es wurden im folgenden Variablen für Schnitte (final cuts) zur Anreicherung des Instanton-induzierten Anteils benutzt: Der Jet-Transversalimpuls, das rekonstruierte Q'^2, die Transversalenergie, die Masse und die Multiplizität des Instanton-Kandidaten. Als beste Strategie zur Bestimmung einer Grenze des Bruchteils an Instanton-induzierten Ereignissen erwies sich eine Anpassung von Sphärizitätsverteilungen.

Die obere Grenze des Bruchteils von Instanton-induzierten Ereignissen in den Daten der tiefunelastischen Streuung, bei einem Konfidenzniveau von 95%, inklusive systematischer Fehler ist

$$f_{\text{lim,Hrw}} = 12\%$$

für das Herwig Monte Carlo Programm.

Einsatz des Ariadne Monte Carlo Programms ergibt:

$$f_{\text{lim,Ari}} = 8.2\%.$$

Diese Grenzen müssen mit dem theoretisch vorhergesagten Wert (QCDINS 1.6) verglichen werden:

$$f = 6.2\%$$

Eine zweite, unabhängige Methode, die auf einer Schnitt-Strategie beruhte, erwies sich als weniger sensitiv und ergab schwächere Grenzen.

Abstract

A limit on the QCD instanton induced cross section has been determined using the data recorded by the ZEUS detector during the year 1997, with a total integrated luminosity of 26pb^{-1}. Deep inelastic scattering events were selected, requiring $Q^2 > 75\text{GeV}^2$ and $x > 10^{-3}$.

Cuts to enrich the instanton fraction (final cuts) have been devised: They are the jet transverse momentum, the reconstructed Q'^2, the transverse energy, the mass and the multiplicity of the instanton candidate. The best strategy to determine a limit on fraction of the instanton candidates among the events after the final cuts has turned out to be a fit to the sphericity distributions.

The upper limit at 95% confidence level of the fraction of instanton events in the DIS sample, including systematic errors, is

$$f_{\text{lim,Hrw}} = 12\%$$

for the Herwig Monte Carlo program.

Using the Ariadne Monte Carlo program yields a limit of

$$f_{\text{lim,Ari}} = 8.2\%.$$

These limits have to be compared to the value predicted by theory (QCDINS 1.6) of:

$$f = 6.2\%$$

A second, independent, method relying on the best strategy of cuts was not as sensitive and gave weaker limits.

Contents

1 Introduction **7**

1.1 Double-Well Potential 7

1.2 Properties of instanton induced events 11

1.3 Status of experimental searches 11

2 ZEUS Data Taking and Reconstruction **13**

2.1 The Calorimeter 13

2.2 Tracking Detector 15

2.3 Trigger 15

2.4 The ZEUS coordinate system 17

2.5 A sample event 17

2.6 Reconstruction 17

3 Physics Simulation **22**

3.1 QCDINS 22

3.2 HERWIG 23

3.3 DJANGOH/Ariadne 24

4 Trigger and event selection **24**

4.1 Trigger 24

4.2 Reconstruction of DIS variables 26

4.3 Offline cuts 26

5 Event reconstruction **27**

5.1 Reference frame 27

5.2 Zufos 27

5.3 Tracks 28

5.4 Jet identification 28

5.5 Q'^2 reconstruction 31

5.6 Comparison of Data and Monte Carlo Simulation 34

6 Identification of Instanton-induced events **41**

6.1 Comparison of Jet Properties 41

6.2 Sphericity 42

6.3 Enhancement of the Instanton fraction (final cuts) 48

6.4 Variation of QCDINS parameters 52

6.5 K^0_S multiplicity 55

6.6 Q'^2 distribution 55

7 Limit on the instanton cross-section **56**
7.1 Reweighting 56
7.2 Limits from fits to the sphericity distributions 57
7.3 Limit via likelihood ratio 60
7.4 Summary of limits determined using sphericity 62
7.5 Limit via cuts 62
7.6 Theoretical prediction 64

8 Systematic errors **65**
8.1 Cut in p_t, Q'^2 65
8.2 Cut in x' 66

9 Conclusion **69**

1 Introduction

The standard model has been very successful at describing data of elementary particle physics [Ell98].

Most of these predictions have been made for the case of weak couplings, so that perturbation theory can be applied.

Instantons are an example of a phenomenon, which is outside the scope of normal QCD perturbation theory, being connected with tunneling transistions between QCD vacua. Instantons are a basic aspect of QCD, which has so far not been verified experimentally. Discovery of instanton induced events would therefore shed light on currently unexplored facets of QCD and the standard model as a whole. The search for instantons has recently been greatly encouraged, because theoretical predictions for the cross sections have now become possible, backed up by Monte Carlo calculations.[RS94, GRS95a, GRS95b, MRS97b, RS98b]

The following section of this thesis will briefly introduce instantons. Then, a description of the experimental setup and the simulation programs will be given. After event selection and reconstruction, the identification of QCD-instanton induced events will be described. Finally, the determined limits on the cross section for instanton induced events will be stated.

The concept of instantons will be introduced in this section via a quantum mechanical example, the double-well potential.

1.1 Double-Well Potential

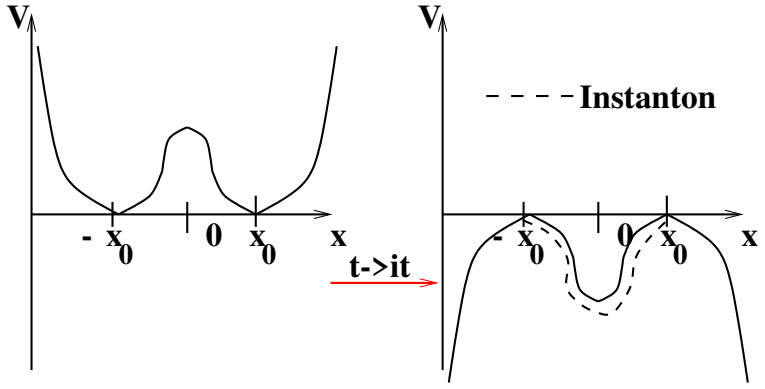

Figure 1: double-well potential. Left: original double-well potential. Right: The same potential after changing Minkowski time t to imaginary time $\tau = it$

Fig. 1(left) shows such a double-well potential. In the classical view, the potential has two separate ground states at $-x_0$ and at x_0. In the quantum mechanical view, these two ground states are mixed due to tunnelling effects.

To be more specific, consider a particle of mass m in this potential. The total energy of the particle is given by

$$E = \frac{m}{2}\left(\frac{\mathrm{dx}}{\mathrm{dt}}\right)^2 + V(x) \tag{1}$$

with the potential energy $V(x) > 0$ except $V(-x_0) = V(x_0) = 0$. For the ground state with $E = 0$ there is no classical solution which allows the particle to go from $-x_0$ to x_0 or vice versa.

Such a transition is however possible in quantum mechanics by tunneling.

This phenomenon can be described classically by transforming the time to imaginary time $t \to -i\tau$. Then eq. 1 becomes

$$-E = \frac{m}{2}\left(\frac{\mathrm{dx}}{\mathrm{d}\tau}\right)^2 - V(x)$$

which for $E = 0$ has the solution

$$\sqrt{\frac{m}{2}} \int \frac{\mathrm{dx}}{\sqrt{V(x)}} = \tau - \tau_0$$

This solution, localized in x, τ must be summed over the (arbitrary) integration constant τ_0. It is called an Instanton solution, because in real time this transition is instantaneous.

This solution helps to compute the transition amplitude T between the two degenerate states at $x = -x_0$ and $x = +x_0$:

$$T = N \int_{x_i}^{x_f} [Dx] e^{-S_\tau(x)}$$

where $[Dx]$ stands for the path integral, N is a normalization constant and the euclidian action is

$$S_\tau = \int d\tau L(x, \tau)$$

With the Lagrangian $L = \frac{1}{2}m\left(\frac{\mathrm{dx}}{\mathrm{dt}}\right)^2 - V(x)$ we have

$$S_\tau = \int_{-\infty}^{+\infty} \left(\frac{1}{2}m\left(\frac{\mathrm{dx}}{\mathrm{d}\tau}\right)^2 + V(x)\right) d\tau$$

and for $E = 0$ we have

$$S_\tau = \int_{-x_0}^{+x_0} dx\sqrt{2mV(x)}$$

The transition amplitude is then proportional to e^{-S_τ}.

Going then to a non abelian Yang Mills theory like QCD things are much more complicated. The vacuum states are characterized by vanishing field strengths; however, the gauge field, A, can still be non-zero: the gauge field A transforms like

$$A'_\mu = U(x)A_\mu U^\dagger(x) - \frac{i}{g}U(x)\partial_\mu U^\dagger(x)$$

where $U(x)$ is a SU3 transformation matrix. The vacuum gauge field is then characterized by

$$A'_{V\mu} = \frac{i}{g}U(x)\partial_\mu U^\dagger(x)$$

All SU3 transformations $U(x)$, which can be connected by a series of continuous transformations are within the same topological class. However, there are (infinitely many) classes of transformations, which can not be so connected. They are members of different topological classes, the corresponding vacua are characterized by a winding number n and separated by an energy barrier, as depicted in fig. 2.

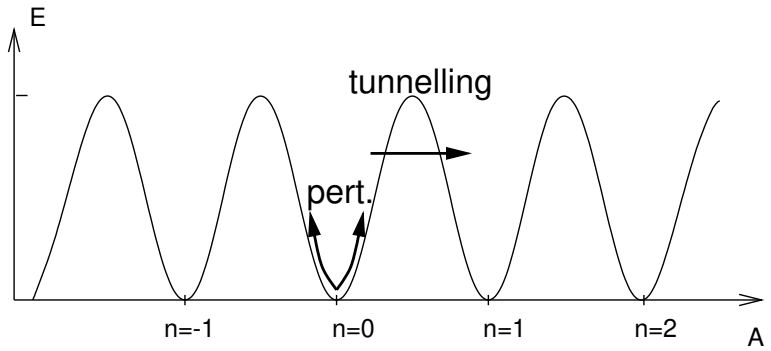

Figure 2: Degenerate vacuum of QCD. Normal perturbation theory is performed around around $n = 0$, tunneling (instanton) transitions are possible with $\Delta n \neq 0$.

Instanton processes are characterized by gauge fields which connect topologically different vacua.
Calculating the transition amplitude T of an instanton process is analogous to the simple quantum mechanical case. The Lagrangian is

$$L_i = \frac{12}{\pi\alpha}\frac{\rho^4}{(x^2+\rho^2)^4} \tag{2}$$

where x^2 is the square of the 4-distance and ρ the size of the instanton gauge field. Integrating over x and ρ leads to the action

$$S_\tau = \frac{2\pi|Q|}{\alpha}$$

where the topological charge Q is the the difference between two succceeding winding numbers $Q = n - (n-1) = +1$ for instantons and $Q = -1$ for antiinstantons and α is the coupling constant. In terms of the fields,

$$Q = \frac{1}{32\pi^2}\int dx^4 G_{\mu\nu}\tilde{G}_{\mu\nu},$$

where $G^j_{\mu\nu} = \partial_\mu A^j_\nu - \partial_\nu A^j_\mu + g f_{jkl} A^k_\mu A^l_\nu$ and $\tilde{G}_{\mu\nu} = \frac{1}{2}\varepsilon_{\mu\nu\rho\sigma}G_{\rho\sigma}$.
The transition amplitude is then $T \propto e^{-2\pi/\alpha}$ and the cross section $\sigma \propto e^{-4\pi/\alpha}$.
An important feature of instantons is that the chirality of the quarks involved in a tunneling process flips. This is described by the axial charge Q_5, which is the difference between the number of right- and left-handed quarks and which is conserved for light quarks in normal QCD. For example, for u-quarks

$$Q^u_5 = u_R + \bar{u}_R - (u_L + \bar{u}_L),$$

where u is the number of u-quarks, $\bar{u}$ the number of anti-u-quarks. One has then, for negligible quark masses:

$$\Delta Q^{(u)}_5 = \Delta Q^{(d)}_5 = \Delta Q^{(s)}_5 = 2Q,$$

where Q is the topological charge. i.e., chirality is violated in instanton processes for light quarks. In normal QCD $\Delta Q_5 = 0$, i.e. chirality is conserved. Summing over the number of all considered quark flavors n_f one has for an instanton transition

$$\Delta Q_5 = 2n_f \cdot Q \tag{3}$$

Figure 3 shows an example of an instanton-induced DIS process.
This diagram is not strictly a Feynman diagram, because it involves an instanton induced transition: the instanton subprocess, symbolically included via a circle, is labelled 'I'. Equation 3 leads to the appearance of $2n_f - 1$ quarks/antiquarks and a number of gluons in the instanton final state .
Although processes with a quark from the proton are possible as well, they are not considered here, because the cross section is much smaller than for gluon initiated processes.[RS98b]
The actual calculation of the cross section can only be carried out within certain restrictions. For example, the integration over the density distribution of the instanton size ρ can only be carried out up to a size of about $0.3f$. This limit is indicated by comparing perturbation calculations with non-perturbative lattice calculations[ST98, RS98a]. Beyond that limit the density from perturbation theory is not reliable. It turns out, that predictions for the cross section have to be

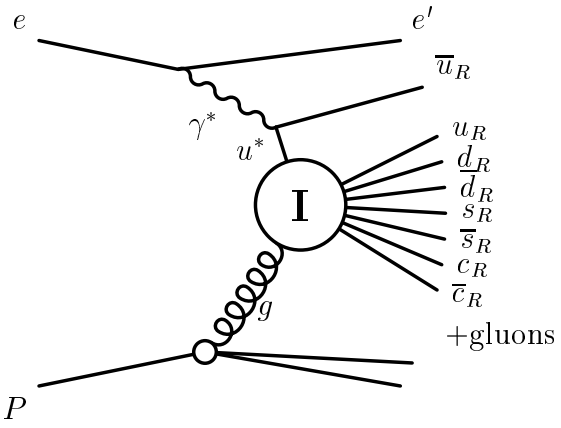

Figure 3: The process diagram of an instanton induced DIS process (adapted from [Kuh97])

confined to values $Q'^2 > 64\text{GeV}^2$, $x' > 0.35$. (See section 3.1 for the meaning of the kinematic variables of the instanton process Q', x'.)

1.2 Properties of instanton induced events

Instanton induced events are expected to have the following properties:

- isotropic

  The form of the instanton Lagrangian (eq. 2) suggests spherical symmetry. The actual calculation confirms this and leads to an isotropic distribution of particles in the instanton center of mass system.

- large number of particles

  See fig. 3 for e.g. $n_f = 3$ flavors (u,d,s) leads to five quarks and antiquarks, which later on fragment to a large number of hadrons.

- flavor democracy

  All n_f quark flavors appear as exactly one quark-antiquark pair.

1.3 Status of experimental searches

Previous limits on the cross section of QCD instanton induced events at HERA have been determined by the H1 collaboration.
One approach used a fit to the K^0 multiplicity distribution[H1 96a]. Since the instanton processes produce at least two strange quarks (here, "quark" includes "antiquark"), an excess in strange mesons is expected. This analysis placed an

upper limit of 0.9nb at the 95% confidence level on the cross section for instanton induced events.

The most stringent limits were determined in a charged particle multiplicity analysis[H1 96b], but still lie significantly above the predicted cross section[CK97]. Not only are two strange quarks required to appear in every QCD instanton induced event, this holds for all flavors that can be considered as massless in the calculations, resulting in the requirement of two each of up, down and strange quarks. Also, in every event a number of emerging gluons is expected, which follows a Poisson distribution with mean approximately equal to 3 in this kinematic region. This led to the expectation of a high particle multiplicity observable in the detector. The multiplicity analysis placed a limit of 0.3nb at the 95% confidence level on the instanton induced cross section.

The simlulation of these events was performed using version 1.4.1 of a simulation package (QCDINS) written by A. Ringwald, F. Schrempp and M. Gibbs [GRS95a, GRS95b]. The results are therefore not directly comparable to those in this thesis, which used a later version (1.60.1); in this version the fiducial regions in x' and Q'^2 shifted.

The latest results on the search for instanton events were shown by S. Mikocki of the H1 collaboration at the DIS2000 conference[Mik00], which showed that after applying cuts to enrich the instanton fraction, a number of events was observed that was above the prediction of simulation programs for normal DIS events, but the excess was of the same order as the difference of the predictions of two different simulation packages.

2 ZEUS Data Taking and Reconstruction

The search for instanton-induced events reported in this thesis has been conducted using data supplied by the ZEUS detector, making mainly use of the Uranium calorimeter and the tracking chambers. In the following the components relevant for this work will be described.
The ZEUS detector is more completely described in [ZEU93] and [ZEU92].

2.1 The Calorimeter

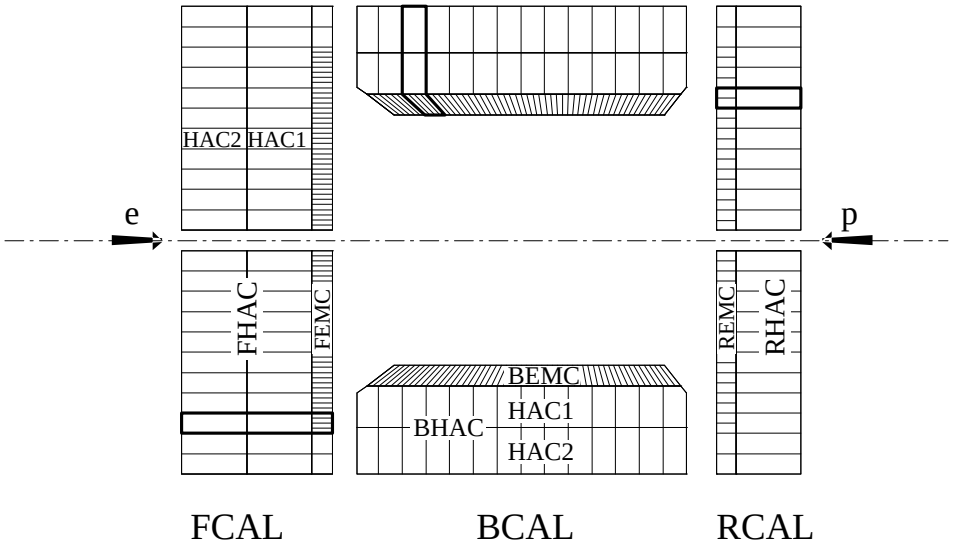

Figure 4: The calorimeter. Inside this (not shown) are tracking chambers.

ZEUS employs a compensating calorimeter that is divided into three major sections (see fig. 4): *FCAL, BCAL* and *RCAL*. The forward region (FCAL, in direction of flight of the protons) covers a polar angle of $2.6° < \vartheta < 36.7°$ with respect to the interaction point (IP). The central region (BCAL) covers the range $36.7° < \vartheta < 129.1°$, and the backward region (RCAL) registers energy depositions in the range $129.1° < \vartheta < 176.2°$.
Every region of the calorimeter is further divided into an electromagnetic (EMC) and one (RCAL) or two (FCAL, BCAL) hadronic sections (HAC). Viewed from the IP, the electromagnetic section lies in front of the hadronic section. The EMC sections have a granularity of $5 \times 20\text{cm}^2$ (FCAL,BCAL) or $10 \times 20\text{cm}^2$ (RCAL); the HAC sections are $20 \times 20\text{cm}^2$ throughout.
The detector cells are built from successive layers of depleted Uranium and scintillator. The light produced in the scintillators is read out by two photomultipliers

for each cell. The use of uranium has two advantages: It can achieve compensation (see below) and the Uranium allows a calibration of the calorimeter due to its constant radiation background.

The calorimeter is built in such a way that the different showering properties of hadrons and electrons/photons are compensated, so that equal energies at the point of entry lead to equal signal heights when integrated over time. A calorimeter with this feature is called **compensating.**. This effect is achieved by an appropriate choice of the thicknesses of the Uranium and scintillator layers of the calorimeter cells.

Cells are combined into towers: in fig. 4 one tower is outlined with a broader line for each detector region. In FCAL, for example, a tower consists of four FEMC cells, one FHAC1 and one FHAC2 cell.

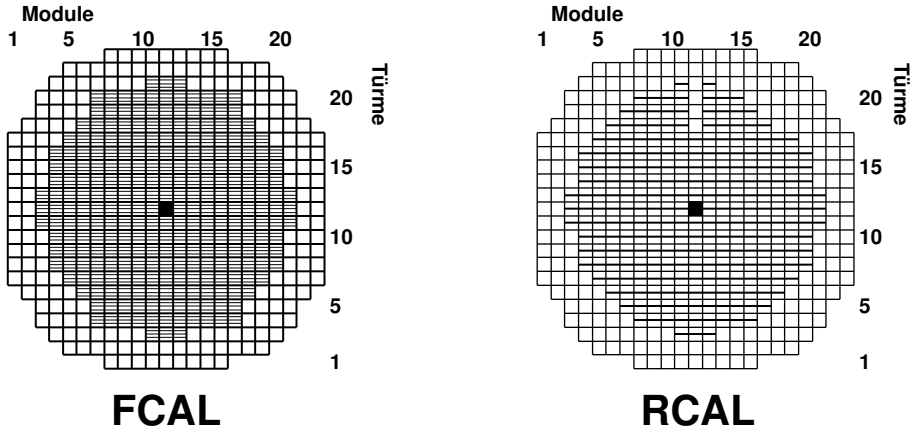

Figure 5: FCAL and RCAL perpendicular to the beam axis. the regions of higher granularity belong to the electromagnetic calorimeter EMC, the surrounding area makes up the HAC0.

FCAL and RCAL are shown in a front view in fig. 5, in which the higher granularity of FCAL can be seen.

As determined by measurements in test beams, the calorimeter achieves a relative energy resolution of

$\sigma_E/E = 0.18/\sqrt{E(\mathrm{GeV})}$ for electrons and

$\sigma_E/E = 0.35/\sqrt{E(\mathrm{GeV})}$ for hadrons.

The absolute energy scale of FCAL and BCAL is known to an accuracy of 3%.

The time resolution of signals from the calorimeter cells is better than 1 ns for energy deposits above 4.5 GeV.

The data from the calorimeter contain background signals from various sources. Contributors are the Uranium's natural activity and noise from read-out electronics. To suppress the influence of background noise, only calorimeter cells are

considered that have more than 60 MeV in the EMC sections and more than 110 MeV in the HAC sections.
A description of the reconstruction software for the calorimeter can be found in [dJ92] and [dK94].

2.2 Tracking Detector

The Central Tracking Detector (CTD) was built to detect charged particles. It is a cylindrical wire chamber that consists of nine superlayers that house eight layers of sense wires each, with a total of 4608 wires[ZEU93]. While five of the superlayers hold wires that are parallel to the axis of the detector, and therefore to the beampipe, the wires of the remaining four are at an angle of $+5°$ or $-5°$, to allow a reconstruction of the longitudinal components of a track's trajectory. The angle of $5°$ was chosen so that the angular resolution in polar and azimuthal angle is approximately equal.
To allow for a momentum measurement, the CTD is kept inside a magnetic field of $B = 1.43T$.
From [HWMN+99], the resolution of the CTD in transverse momentum is

$$\frac{\sigma_{p_\perp}}{p_\perp} = 0.0058 p_\perp \oplus 0.0065 \oplus 0.0014/p_\perp$$

where $p_\perp$ is measured in GeV. The three terms denote the resolution of the hit positions, smearing from multiple scattering within the CTD and scattering before the CTD, respectively.

2.3 Trigger

At 96ns between bunch crossings of the electron and proton beams, there is a very high rate of potential events. To select interesting events, the rate is reduced by three trigger levels. The complete trigger and data acquisition system is shown in fig. 6.
The first level trigger (FLT) reduces the rate of events to 1kHz. It consists of local FLTs for the different components of the detector, the results of which are then combined in a global FLT (GFLT). At the FLT level, only very simple information like neighbouring energy deposits in the calorimeter is available.
The second level trigger (SLT) can already combine the information from FLT level into more complex structures, e.g. the information from different sections of the calorimeter is combined [Dep94]. The SLT reduces the event rate to about 100Hz and consists of a combination of local component SLTs and a global SLT, analogous to the FLT.
Before entering the third level trigger (TLT), information from the various components is combined by an Event Builder, in order to allow the TLT to base its

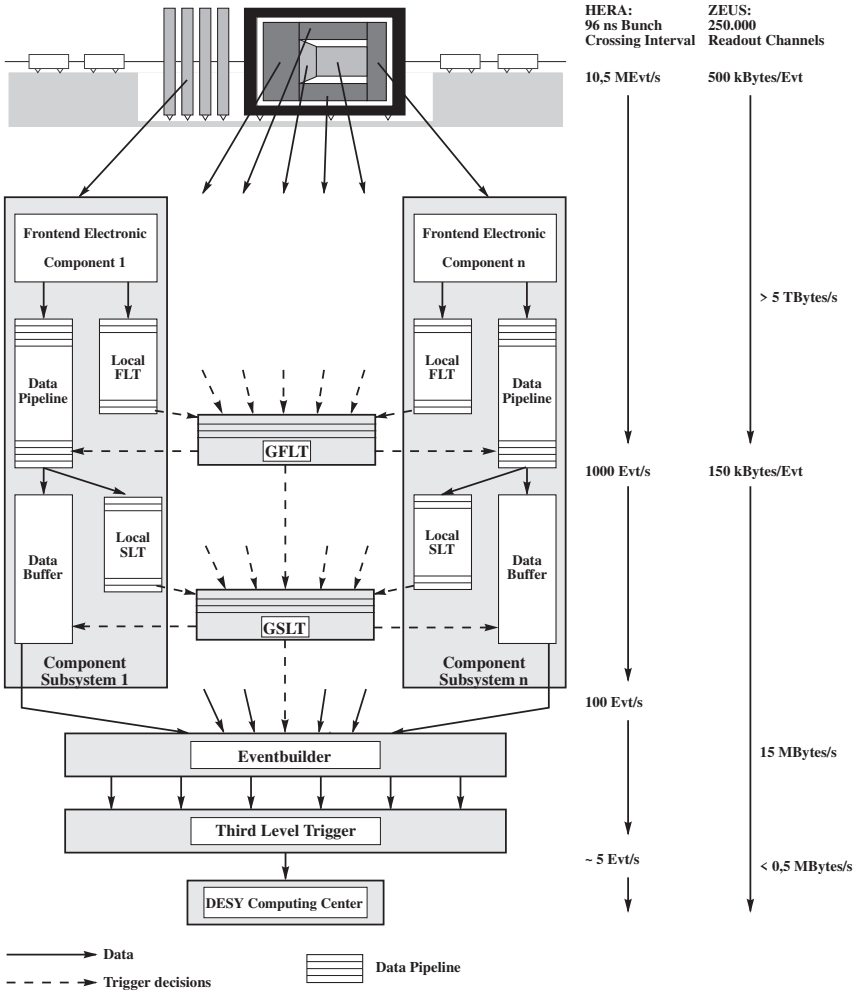

Figure 6: The ZEUS trigger and data acquisition system. Events are filtered in a series of triggers. The first level trigger (FLT) reduces the event rate from 10MHz to 1kHz. The second level trigger (SLT) reduces this to 100Hz and the third level trigger (TLT) reduces this to 5Hz. This corresponds to less then 500kByte per second to be stored on magnetic media.(adapted from [Ohr96])

decisions on various aspects of the complete event. The TLT reduces the event rate further to about 5 events per second, which can finally be stored on magnetic tape inside the DESY computing center.

2.4 The ZEUS coordinate system

In descriptions of the ZEUS detector, a right-handed coordinate system is used, with the horizontal x-axis in the direction of the center of the storage ring, the y-axis pointing upward and the z-axis in the direction of flight of the protons. The origin of the coordinate system is identical to the nominal interaction point, where electrons and protons are made to collide.

The polar angle is denoted by ϑ and the azimuth by φ; the angle ϑ is measured against the direction of flight of the protons.

2.5 A sample event

Detector data can be visualized with the program LAZE[Dor91]. An example event display can be found in fig. 7. It shows a simulated QCD instanton induced event as seen by the ZEUS detector simulation. In the left half a Z-R projection of the detector can be found. This projection divides the detector into two halves, here with positive and negative y. In each half, the energy deposits in the calorimeter are summed over the azimuth φ at fixed z and entered into a single cell in the graphical representation. Tracks reconstructed in the central tracking detector are continued into the calorimeter.

At the bottom right is a projection of the tracking chamber on the x, y-plane. In this type of projection one looks into the detector along the beam axis, so that only the x and y coordinates are used in the drawing. One can see the high multiplicity of tracks of an instanton induced event.

At the top right finally a projection of the calorimeter into the $\eta - \varphi$ plane can be found (the pseudorapidity η is defined in section 5.4). Here the electron can be found easily by sharp, high peak in the lower left and the jet resulting from the $\bar{u}_R$ quark in fig. 3 is at approximately the same η as the electron, but at higher $\varphi \approx 330°$. The decay products of the instanton subprocess make up the rest of the energy depositions, along with fragmentation products of the proton.

2.6 Reconstruction

After having been written to magnetic tape during luminosity runs, all data undergoes a process of **reconstruction** in which the detector signals are converted into physical quantities that can be used for analyses.

The reconstruction of events detected by ZEUS is a complex task due to the number of components that need offline reconstruction and to the large amounts

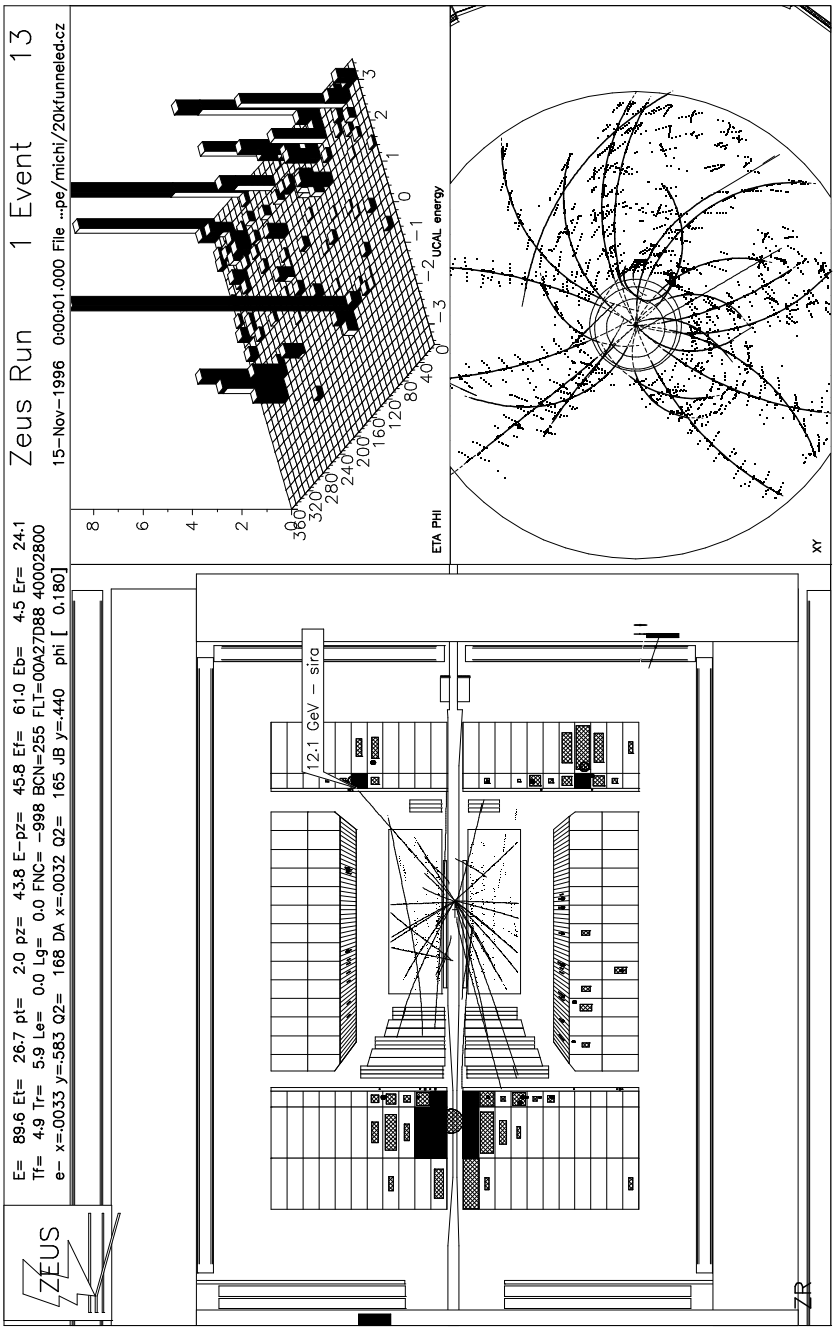

Figure 7: A simulated QCD instanton induced deep inelastic scattering event as seen by the ZEUS detector simulation.

of data that need to be processed.
The task is facilitated by the fact that the same program (zephyr) is used for reconstruction on independent sets of data split into files. This allows the reconstruction to be distributed among many processors on one or more machines.
Since fall 1998, reconstruction is done entirely on Linux PCs, after a migration period from a multiprocessor SGI Challange. Data is transferred from tape to a spool area, on which the PCs can work via the network file system nfs. One PC is set aside to distribute the work, transfer the files to the spool area, combine and transfer the results back to tape or to a batch processing facility (zarah) for quick access.
The following sections will describe the hardware and software used in the reconstruction process.

2.6.1 Hardware

The PC farm used for reconstruction consists of 17 PCs running under Linux, Kernel 2.0.33. The PCs have Pentium Pro processors running at 200MHz, 64MB of memory, and 2GB of local diskspace. They communicate among each other via Fast Ethernet.

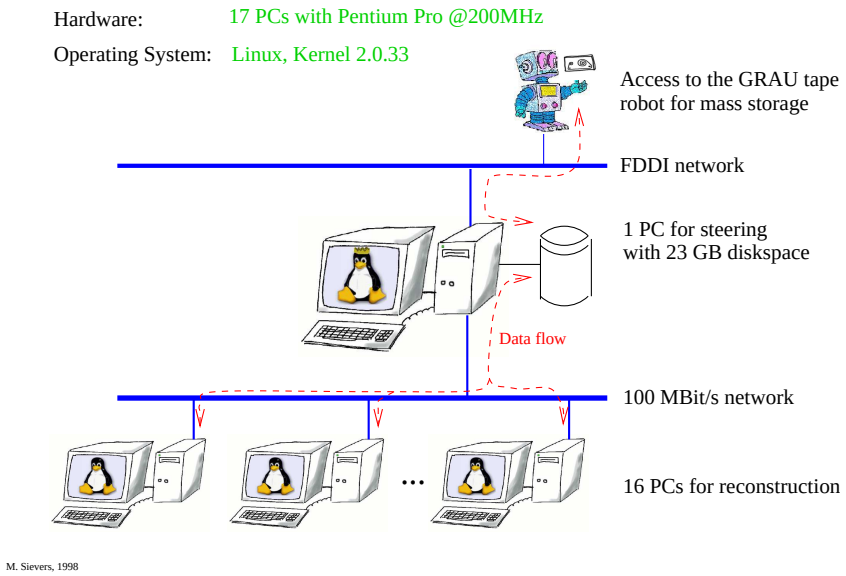

Figure 8: Schematic of the PC farm

One of the PCs (called **master**) is set aside for the steering of the other PCs (**clients**) and for transfering (staging) data files from and to tape. This PC has an additional FDDI card which connects it to the batch facility zarah and the tape

robot (GRAU). The master is equipped with an array of three 9GB harddisks, which is read from and written to by the clients during reconstruction. The array is configured as a RAID level 0 array, that is, the three disks appear as a single logical volume and the access is organized in **stripes** across the disk, to increase sequential reading speed. Figure 8 shows schematically how the PC farm is set up. The 16 client PCs are at the bottom, the master is in the middle.

The PCs are set up in the central computing center and respond to the names of zenith20–zenith36. The master is called zenith35.

2.6.2 The reconstruction process

The data is organized in **runs**, the data from which are organized into one or more **files**. Files are the most important units in the reconstruction process.

As each file is processed, it is always in a certain **state**, depending on whether it is just being staged, waiting for a free processor, or being written to tape. The state of each file is expressed by its filename being present in a corresponding directory. As an example, if file `FILE_A` has already been copied from tape to disk and is waiting to be processed, it is in the state *TOPROCESS*. This is equivalent to a file with name `FILE_A` being present in the directory `rec_dirs/TOPROCESS`. (The real file `FILE_A` that is waiting to be processed, resides in an input directory on the RAID array). In this way, different scripts can communicate by setting file names in directories. Care has only to be taken in order to avoid race conditions.

The different states that a file goes through during the reconstruction of its data is shown in fig. 9. The nominal transitions follow the circle clockwise, but at any stage an error may occur and can be corrected manually.

2.6.3 Configuration

The reconstruction is steered by a configuration file `ctrl`, at this time located at `zenith35:/data3/dbrec/control/ctrl`.

In this file, the information needed to run the reconstruction is contained. This information includes:

- Name and location of the reconstruction program
- location of list of files/runs to be reconstructed
- location of list of events not to be reconstructed (veto list)

2.6.4 Managers

The tasks that need to be handled during reconstruction are divided among several scripts, i.e. Unix operation programs, called **managers**. The main managers

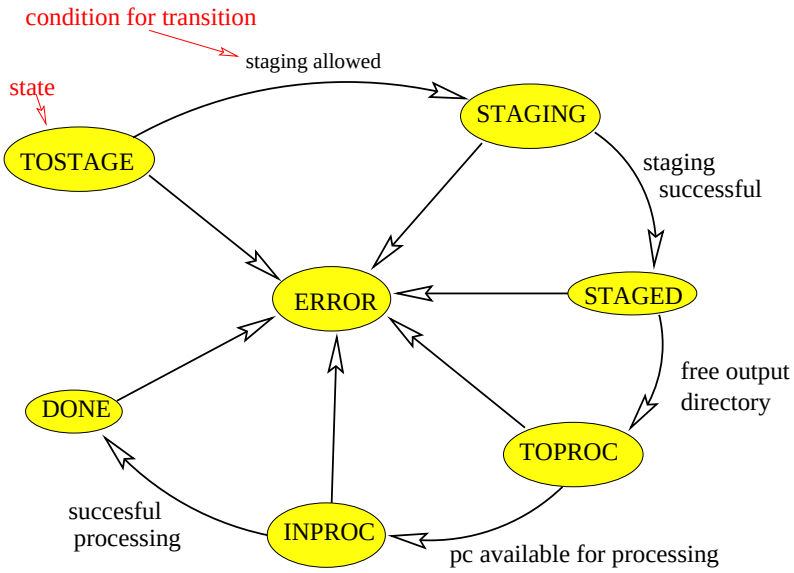

Figure 9: File states during reconstruction. Shown are the different states (inside ellipses) and the conditions for transition to the next state. During its reconstruction life, a file is marked as ready to stage, being staged, completely staged, ready to process, in process and finally done. Errors that can occur at any time are caught and documented for manual intervention.

are the **directory manager** (dir_mgr), the **file manager** (file_mgr), and the **run manager** (run_mgr). In the following, the tasks of these managers will be briefly described.

1. Directory manager

   The directory manager assigns input directories to files that are to be reconstructed ($TODO$), and schedules them for staging ($TOSTAGE$). When they are $STAGED$, the directory manager assigns them an output directory and sets their state to ready to process ($TOPROC$).

2. Run manager

   The run manager supervises copying of files from tape to disk, starts the actual reconstruction processes and sees to it that the reconstruction results are written to tape and, where applicable, to the batch facility zarah. Finally, the state of a file is changed to $DONE$ when it is successfully reconstructed.

3. File Manager

   The file manager restarts not running managers if they are needed and builds a list of new runs, when they become available.

The reconstruction steering has been successfully ported from an SGI multiprocessor machine to a Linux PC farm environment.

3 Physics Simulation

In order to search for instanton-induced events in deep inelastic scattering, this analysis makes intensive use of programs that simulate physics events. These programs are often called '**Monte Carlo**' programs due to the probabilistic methods employed, involving the frequent use of random numbers employed to determine which process of several possible ones will 'happen' in any event.

Several Monte Carlo programs exist, depending on the physics processes that are to be analyzed. In this analysis, the program QCDINS is used to model the instanton-induced processes and HERWIG is used to model the normal DIS events. Ariadne is used as a cross-check to model normal DIS events. Existing sets of simulated events with $Q^2 > 4\text{GeV}^2$, $Q^2 > 10\text{GeV}^2$, $Q^2 > 40\text{GeV}^2$ and $Q^2 > 70\text{GeV}^2$ were used, the generation cuts in x were set varyingly at $x > 10^{-4}$ and $x > 10^{-3}$. (In a frame of reference where the proton speed is $v \approx c$, x is the momentum fraction that the struck parton carried.) Throughout this analysis, only events with $Q^2 > 75\text{GeV}^2$ and $x > 10^{-3}$ were used, so that no reweighting for the generated events was needed.

3.1 QCDINS

For the simulations of QCD-instanton induced events in deep inelastic electron-proton scattering the Monte Carlo package QCDINS[GRS95c] was used, in its version 1.6.1.

It is designed as an add-on hard process generator interfaced to HERWIG, and the newest version 2.0 also provides an interface to JETSET for fragmentation.

It includes the theoretically predicted rate and theoretically derived characteristics of the final state: flavor democracy[tH76a, tH76b, tH78, tH86], isotropic production[GRS95a, MRS97a] of final state partons and energy weight factors different for gluons and quarks. The final state corresponds to $2n_f$ (here, $n_f = 3$) quarks plus antiquarks and $\mathcal{O}(1/\alpha_s) \approx 3$ gluons, with the number of gluons following an approximate Poisson distribution.

The program generates events in 5 steps (refer to fig. 10 for the meaning of the variables):

1. Generate Q'^2 (virtuality of the quark entering the instanton subprocess), x' (x equivalent for the instanton subprocess), ξ (momentum fraction of the gluon), x, y_{Bj}

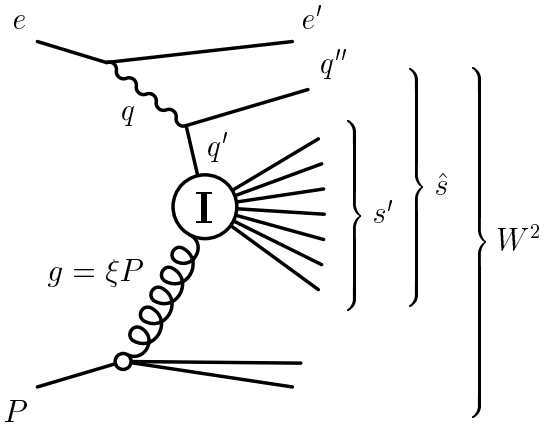

DIS variables:
$Q^2 = -q^2 = -(e - e')^2$
$x = Q^2/(2P \cdot q)$
$W^2 = (q + P)^2 = Q^2(1 - x)/x$
$\hat{s} = (q + g)^2$
$\xi = x(1 + \hat{s}/Q^2)$

Variables of the instanton subprocess:
$Q'^2 = -q'^2$
$x' = Q'^2/(2g \cdot q')$
$s' = (q' + g)^2 = Q'^2(1 - x')/x'$

Figure 10: Kinematical Variables of the instanton process. In addition to the variables Q^2, x, W^2 that are defined as in normal DIS, there are additional variables Q'^2, x' that are defined analogously and describe the instanton subprocess. (Adapted from [Kuh97])

2. generate g, q, q', q'', which denote the four-momenta of the gluon, the virtual photon, the quark connecting photon and instanton process and the current quark, respectively.

3. generate final state quarks and gluons

4. establish color and flavor connections

5. perform hadronization using HERWIG (or JETSET in version 2.0)

3.2 HERWIG

It is important to use the physics simulation program HERWIG[M+92] (Hadron Emission Reactions With Interfering Gluons) to model the normal DIS events because the instanton event generator is embedded into HERWIG; QCDINS uses HERWIG to perform the generation of hadrons from the initial state partons. In order to assure that we are not merely identifying a difference in this stage of event generation between HERWIG and Ariadne, HERWIG is used to model normal DIS events as well.

HERWIG is a general-purpose Monte Carlo and allows to model lepton-lepton, hadron-hadron and mixed hard processes. Initial and final state radiation is modelled using the parton-shower approach and includes colour coherence effects.

As with other Monte Carlo programs, the justification for this program lies in the fact that a process like the scattering of an electron off a proton can be factored into different subprocesses: Initial and final state radation, the hard subprocess and hadronization.

The hard process can directly be computed by perturbation theory from the matrix elements.

Before and after the hard process occurs, the partons involved may radiate other partons which are limited in virtuality by the scale Q.

The partons, bearing colour charges, evade direct observation. Therefore, HERWIG also includes a hadronization process that models the converstion from partons to final state hadrons, which can then be fed through a simulation of the ZEUS detector. Hadronization models are determined phenomenologically and specific to different kinds of Monte Carlo programs.

Hadronization in HERWIG is performed using a cluster hadronization model. After the perturbative processes, all remaining gluons are split into light (u and d) quarks-antiquark pairs. Clusters of color singlets are then built and the clusters fragmented into hadrons, with momentum exchanges where necessary to generate correct masses for the outgoing hadrons.

3.3 DJANGOH/Ariadne

In addition to Herwig, the Monte Carlo package DJANGOH[Spi93a] has been used to model inclusive neutral current events.

DJANGOH is an interface to the event generators HERACLES[Spi93b] to include radiative effects, LEPTO[IER97] to simulate the hard processes and Ariadne[Lön92] to simulate the parton cascades.

Hadronization is performed using the Lund string model[A$^+$83] as implemented in JETSET[Sjö94]. In this model, color strings are connected to the final state partons, with gluons represented as kinks in the strings. During the hadronization phase, the partons move in random directions, thus stretching and finally breaking the strings. This corresponds to the creation of a quark-antiquark pair from the vacuum. This process is iterated until no more breaking is possible.[Okr99]

4 Trigger and event selection

4.1 Trigger

This analysis is based on the data that has been collected by the ZEUS experiment during the year 1997. HERA ran with protons of 820GeV and positrons of 27.5GeV. The integrated luminosity, on which these data are based, was $\mathcal{L} = 26.0\text{pb}^{-1}$.

For both data and physics simulation, the following cuts have been applied:

On the first trigger level, it was required that any of the DIS trigger slots 28, 30, 40, 42, 43, 44, 46 and 47 had fired.These represented the following requirements, at least one of which had to have occurred:

- an isolated electron must have been identified in FCAL or BCAL; in addition, a track must have been found in the CTD
- an isolated electron must have been found in RCAL; in addition, more than 2 GeV must be found in the EMC section of RCAL.
- the total energy in the electromagnetic sections must be greater than 15GeV
- the total transverse energy must be greater than 15GeV
- the total transverse energy must be greater than 12GeV and at least one track must have been found in the CTD
- Energy in REMC must be greater than 3.4GeV or greater than 4.8GeV in the BEMC, if a track is found.
- an isolated electron must have been found, additionally the energy in REMC must be greater than 2GeV, or a signal in SRTD and a track must have been found, or the total transverse energy must be greater than 18GeV

On the second trigger level, every event fullfilled the requirement that the DIS bit 1 be set, which is the main DIS filter. This corresponds to requiring

- more than 2.5GeV in the REMC or BEMC, or more than 10GeV in the FHAC or FEMC and
- $E - P_z + 2 * E_{\mathrm{lumi}\gamma} > 29\mathrm{GeV}$, where $E_{\mathrm{lumi}\gamma}$ is the energy entry in the luminosity measurement detector. E is the total energy deposited in the calorimeter. From the energy deposition and the unit displacement vector of the corresponding calorimeter cell from the event vertex, a three-vector is constructed; P_z is the sum of the longitudinal components of these vectors, the positive direction of the z-axis being the direction of flight of the proton. The momentum contributed by the proton is approximately equal in size and sign to the energy contributed by it (modulo a factor of c), so that mainly the electron contributes to this observable. For the electron, $E \approx -P_z$, so that a normal DIS event with electron contained in the detector has $E - P_z \approx 55\mathrm{GeV}$.

On the third trigger level, the DIS03 trigger bit has been required, corresponding to:

- An electron with an energy above 4 GeV has to be identified.The present analysis required an electron identified by the SINISTRA algorithm. This will be described in the next section.
- The electron has to be farther away from the beampipe than 25cm.
- $E - P_z$ has to exceed 30 GeV.

4.2 Reconstruction of DIS variables

A first step in the analysis of an event of deep inelastic scattering is the identification of the scattered electron. In this analysis, the electron finder SINISTRA[ACS95] is used for this task. It analyses clusters of energy depositions and makes use of calorimeter quantities such as the ratio of energy deposited in the electromagnetic calorimeter and the total deposited energy and the shower profile. To optimize the identification, a neural network is employed.

In addition to identifying the electron, the Lorentz invariant variables Q^2, x, y that describe the kinematics of the process must be reconstructed.

The variables x and y are reconstructed by the "double angle" method [BEK91], using the polar angle θ of the scattered electron with respect to the proton beam direction and the hadronic angle γ defined below. In the quark-parton-model, γ is the angle under which a single struck parton would emerge from the process.

$$\begin{aligned}
\cos\gamma &= \frac{P_x^{\mathrm{tot}\,2} + P_y^{\mathrm{tot}\,2} - (E^{\mathrm{tot}} - P_z^{\mathrm{tot}})^2}{P_x^{\mathrm{tot}\,2} + P_y^{\mathrm{tot}\,2} + (E^{\mathrm{tot}} - P_z^{\mathrm{tot}})^2} \\
Q^2_{\mathrm{DA}} &= 4E_e^2 \frac{\sin\gamma(1+\cos\theta)}{\sin\gamma + \sin\theta - \sin(\theta+\gamma)} \\
x_{\mathrm{DA}} &= \frac{E_e}{E_p} \frac{\sin\gamma + \sin\theta + \sin(\theta+\gamma)}{\sin\gamma + \sin\theta - \sin(\theta+\gamma)}
\end{aligned}$$

where P_x^{tot}, P_y^{tot}, P_z^{tot}, E^{tot} are the sums of the momentum components and energy of all calorimeter cells not assigned to the electron. To assign a calorimeter cell a momentum, its energy is used as magnitude in combination with a unit vector in direction of the cell's vectorial displacement from the interaction point and E_e and E_p are the energies of the incoming lepton and proton, respectively. Q^2_{DA} and x_{DA} are the reconstructed Q^2 and x via the double angle method, respectively.

The variable y is reconstructed via the Jacquet-Blondel method [BEK91]:

$$y_{\mathrm{JB}} = \frac{E^{\mathrm{tot}} - P_z^{\mathrm{tot}}}{2E_e}$$

4.3 Offline cuts

In addition to the cuts performed at the third level trigger, further cuts have been performed in the offline computations.

- $Q^2_{DA} > 75GeV^2$, $x_{DA} > 10^{-3}$: to be safely in the fiducial region of the instanton Monte Carlo
- $0.05 < y_{JB} < 0.95$ to reduce contamination by photoproduction events

- $35GeV < E - P_z < 65GeV$ to reduce radiative events and photoproduction
- Energy of the scattered electron $E_{ele} > 10$GeV
- $d_{\text{ele}} := \sqrt{x_{\text{ele}}^2 + y_{\text{ele}}^2} > 25$cm, where x_{ele} and y_{ele} are the horizontal and vertical displacement of the electron from the center of the beampipe.

In the following, the term "offline cuts" will refer to these cuts.

5 Event reconstruction

Before data can be analyzed to determine e.g. the content of instanton-induced processes, several quantities that describe the observed events have to be computed.
To determine the kinematic variables Q'^2 and x' (see fig. 10) of the possible instanton subprocess, a jet has to be found that originates from the current quark, i.e. the quark struck by the virtual photon. In combination with the electron information, knowledge about the jet allows the computation of Q'^2. The determination of x' is more difficult, as it involves separating the decay products of the gamma-gluon system from the proton remnant. It is also sensitive to loss of information from particles escaping undetected at low angles to the beampipe.

5.1 Reference frame

The ideal rest frame to analyze instanton-induced events would be the center of mass frame of the virtual photon and the gluon entering the reaction ($\gamma^* g$-frame). However, due to difficulties in reconstructing the momentum of the gluon, the corresponding Lorentz transformation is not accurate enough.
Instead, the hadronic center of mass (HCM) system, i.e. the rest frame of the virtual photon and the proton ($\gamma^* p$-frame), was used as the rest frame of choice for this analysis. This system can be identified with significantly more ease, and differs from the gluon-photon system only by a longitudinal Lorentz boost along the direction of the proton, thus leaving momentum components transverse to the $\gamma^* p$ axis invariant.

5.2 Zufos

In the past, analyses have focused on exclusive use of either the tracking information of the CTD or energy information of the calorimeter. As an effort to combine both kinds of information to improve the accuracy of the measurements, zufos have been created. They are described at length in [Bri98].

The concept behind zufos is to use tracking information instead of calorimeter information whenever a gain on energy resolution can be achieved. In this way, low energy charged particles that do not reach the calorimeter are included naturally in the analysis.

As a preparatory step, tracks and calorimeter entries associated to the reconstructed electron are removed and the remaining calorimeter entries are grouped into cone islands, which is a way of combining a cluster of neighboring cells that have registered an energy deposition.

Next, the tracks are extrapolated to the calorimeter and matched to the cone islands. If energy deposits are associated to only one track and also the momentum resolution of that track is better than the energy resolution of the calorimeter, the information from the track is taken instead of the calorimeter information.

A positive consequence of using zufos is that the influence of inactive material between the tracking chamber and the calorimeter is greatly reduced, especially for low-energy particles.

For this analysis, zufos have been used instead of tracks or calorimeter cells, unless otherwise stated.

5.3 Tracks

Not all tracks that are identified during the reconstruction phase can be taken for analyses, instead quality requirements have to be made to the tracks.

The tracks used in this analysis have passed the following requirements:

- the track has to be associated to a primary or a secondary vertex, as determined by the reconstruction process.
- the track has to have at least 21 wire hits.
- (the track has to reach at least superlayer 3) **OR** (superlayer 1 of the CTD, if additionally an FTD segment is included in the track).
- the track has to have a transverse momentum $p_t > 0.15\text{GeV}$

In the following, 'track' always refers to a track that passed these quality cuts.

5.4 Jet identification

To identify a jet candidate for the current quark fragmentation products, the k_t algorithm[C$^+$93] is used to find jets in the hadronic final state.

The k_t algorithm is a cluster algorithm that clusters all final state hadrons into jets. It defines a measure for the transverse momentum d_{ij} of hadron i with respect to hadron j. For each hadron i, the program computes d_{ij} and additionally

the transverse momentum with respect to the proton beam d_{ib}. If there is a hadron j, for which d_{ij} is a minimum, hadrons i and j are merged into a jet, which is then reinserted into the list of hadrons to participate further in the merging process. Should d_{ib} be smaller than any d_{ij}, the particle is assigned to the proton remnant. This process is iterated until the minimum transverse momentum is above a cut-off value.

In this analysis, the k_t algorithm was used to cluster zufos, using a transverse momentum measure $d_{ij} = \min(E_t^i, E_t^j)^2 \cdot (\Delta\eta^2 + \Delta\varphi^2)$. E_t^i is the transverse energy of zufo i, $\Delta\eta$ is the difference in pseudorapidity η of the two zufos; the pseudorapidity is a monotonic function of the polar angle θ of a particle to the beam axis: $\eta = -\ln\tan(\theta/2)$. $\Delta\varphi$ is the difference in azimuth of the zufos i and j. The jet momenta are reconstructed using the KTINCL routine of the k_t algorithm, according to an inclusive jet definition by Ellis and Soper. This definition determines when to stop merging hadrons into a jet.

5.4.1 Jet candidate selection

If more than one jet is found, a best candidate for the current quark jet has to be identified.

Two different methods of identifying the jet belonging to the current quark have been evaluated. The first one, named "High", simply assigns the jet with the highest transverse momentum in the HCM to the current quark. The second method, named "etamean", additionally requires us to consider only jets that have a pseudorapidity η_{jet} larger than the E_t^{zufo}-weighted mean pseudorapidity $\bar{\eta}$ of all reconstructed zufos, where E_t^{zufo} is the transverse energy of the zufo:

$$\begin{aligned} \eta_{jet} &\geq \bar{\eta} \\ \bar{\eta} &= \frac{\sum_{\text{zufos}} E_t^{\text{zufo}} \cdot \eta^{\text{zufo}}}{\sum_{\text{zufos}} E_t^{\text{zufo}}} \end{aligned}$$

where the sums run over all zufos. This method is described in [CGRS99a].

For both methods, the efficiency of correctly tagging the jet closest to the current quark was determined with the instanton Monte Carlo. The result is given in table 1. The efficiencies for both methods have been calculated: once for all events that passed the offline cuts, and once only for events with a jet with a transverse momentum p_t above 4 GeV. The transverse momentum is defined as the momentum component perpendicular to the beam axis and is taken directly from the clustered zufos, without further corrections. The efficiency is defined as

$$\varepsilon = \frac{\text{number of events with a correctly identified jet}}{\text{total number of events}}$$

where correctly identifying the jet means that the jet tagged as the current jet is the one closest to the current quark in the η-φ-plane. In the case of no p_t cut,

all events with at least one jet are counted in the "total number of events" and in the case of a p_t cut at 4GeV, only those events with at least one jet with a p_t above 4GeV have been counted.

Method	ε
High	57.1%
$p_t > 4$ GeV,High	83.7%
etamean	53.9%
$p_t > 4$ GeV, etamean	**94.7%**

Table 1: Efficiency of tagging the correct current jet candidate, calculated using QDINS.

As can be deduced from this table, the preferable method is the "etamean" method with a lower limit on the jet p_t of 4GeV.
In the following, this will always be the method used to identify the current jet candidate.

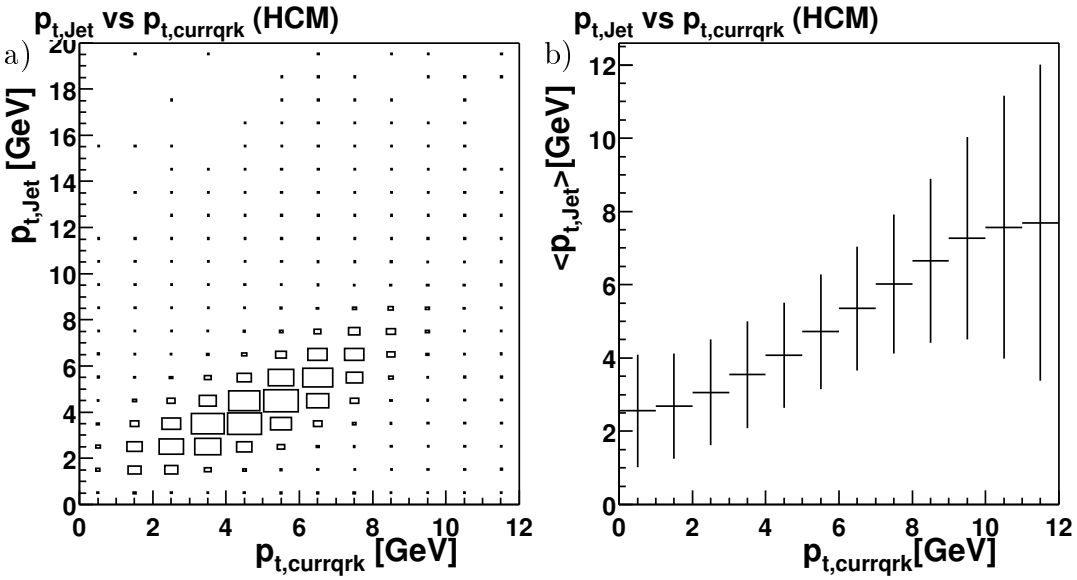

Figure 11: a) Jet p_t vs Current Quark p_t, the area of the boxes is proportional to the number of events. b) Mean jet p_t vs Current Quark p_t. The error bars show the standard deviation of the jet p_t.

The effects of the choice of 4GeV as a lower limit to the jet p_t can be seen by looking at the p_t of the current jet candidate vs the p_t of the current quark.
In fig. 11a), the jet p_t is plotted against the current quark p_t; the area of the

boxes is proportional to the number of events. In fig. 11b), the *mean* jet p_t is plotted against the current quark p_t, the vertical error bars show the standard deviation of the jet p_t. Starting at 4 GeV, there is a good correlation between the mean jet p_t and the current quark p_t. Above 9 GeV, it flattens out; this is probably due to misidentified events yielding a low transverse momentum of the jet.

The lower jet p_t limit of 4GeV is a compromise between a good efficiency of tagging the correct jet candidate and loss of statistics. This lower limit excludes approximately 40% of all events generated by the instanton MC.

5.5 Q'^2 reconstruction

The parameters Q'^2 and x' of the instanton subprocess are important for comparing the experimental finding to theoretical predictions, because the cross section depends strongly on the two. All methods devised during the work on this analysis to reconstruct x' led to rather inaccurate results. (See fig.34 for a comparison of the reconstrcuted x' and the generated x'.) The reconstruction of Q'^2 however yields a better accuracy and will therefore be described in this section.

The formula, according to which the variable Q'^2 is calculated, is the following:

$$Q'^2 = Q^2 + 2qq'' - q''^2 \tag{4}$$

where q is the four-momentum of the virtual photon, q' is the four-momentum of the virtual quark that enters the instanton process, q'' is the four-momentum of current quark, $Q^2 = -q^2$ and $Q'^2 = -q'^2$ (see also fig. 10 on page 23).

In the center of mass system of the virtual photon and the proton, this can be written in the following manner, using reconstructed values:

$$Q'^2 = Q^2 + E_\gamma \sum_{i \in Jet} E_i - p_{z,\gamma} \sum_{i \in Jet} p_{z,i} - M_{jet}^2 \tag{5}$$

where E_γ and $p_{z,\gamma}$ are the energy and longitudinal momentum of the virtual photon (derived from the four-momentum of the incoming k and scattered electron k' by $E_\gamma = k_0 - k'_0$ and $p_{z,\gamma} = k_3 - k'_3$), E_i is the energy of zufo i belonging to the current jet candidate, $p_{z,i}$ is its longitudinal momentum and $M_{\text{jet}} = \sqrt{(\sum_{i \in Jet} E_i)^2 - \sum_{j=x,y,z} (\sum_{i \in Jet} p_{j,i})^2}$ is the mass of the jet. (Energies are measured in GeV, momenta in GeV/c, factors of c are omitted.)

The true value of Q'^2 can be reconstructed by different methods Q'^2, some of which will be compared in the following paragraphs. For four ways of identifying the jet and three ways of reconstructing Q'^2 have been inspected.

Either all zufos that are assigned to the current jet candidate by the k_t algorithm can be used to calculate Q'^2, or the choice may be restricted to particles within a cone of fixed radius R around the jet direction, where $R = \sqrt{\Delta\eta^2 + \Delta\varphi^2}$ is the

distance of a zufo to the jet direction in the η-φ-plane. This procedure is along the lines of [Ger98], where it was found that a cone algorithm with a small radius yields best results for the determination of Q'^2.
The possibilities considered to select the zufos belonging to the jet were:

Kt: zufos as assigned to the current jet candidate by the k_t algorithm

Large: zufos within a cone of radius $R = 1.4$ around the direction of the current jet candidate

Medium: zufos within a cone of radius $R = 1.0$ around the direction of the current jet candidate

Small: zufos within a cone of radius $R = 0.7$ around the direction of the current jet candidate

To reconstruct Q'^2 from detector information, one can rely on information from the reconstructed virtual photon only, or take into account data from the scattered hadronic system, as used in reconstructing the kinematic variables by the double angle method. The explored methods for computing Q'^2 are:

DA: Information from the double angle method:

$$Q'^2 = Q_{DA}^2 + \frac{W_{DA}^2 - Q_{DA}^2}{W_{DA}} \cdot \sum_{i \in \mathrm{Jet}} E_i - \frac{W_{DA}^2 + Q_{DA}^2}{W_{DA}} \cdot \sum_{i \in \mathrm{Jet}} p_{z,i} - M_{\mathrm{Jet}}^2 \quad (6)$$

where $W_{DA} = \sqrt{Q_{DA}^2 \cdot (1 - x_{DA})/x_{DA} + m_p^2}$ and m_p is the mass of the proton.

Gamma (γ): using only the electron variables to reconstruct the virtual photon:

$$Q'^2 = Q_\gamma^2 + 2 \cdot q_\gamma p_{\mathrm{Jet}} - M_{\mathrm{Jet}}^2$$

where $q_\gamma = (E_\gamma, \vec{p}_\gamma)$, $Q_\gamma^2 = -q_\gamma^2$ and p_{Jet} is the four-momentum of the current jet candidate.

Mix: Q^2 from double angle method, otherwise gamma method:

$$Q'^2 = Q_{DA}^2 + 2 \cdot q_\gamma p_{\mathrm{Jet}} - M_{\mathrm{Jet}}^2$$

Using the instanton MC, the relative error of the variable Q'^2 has been plotted in fig. 12. The method to reconstruct Q'^2 in this figure is the double angle ('DA') method, using information from the jet with the smallest cone ('Small'), and a cut on the p_t of the current jet candidate of $p_{t,\mathrm{Jet}} > 4\mathrm{GeV}$ has been applied. The combination of 'DA' method and 'Small' jet proved to have the best resolution and will be used throughout the rest of this analysis to determine Q'^2.
Fig. 12 shows that there is a tail to large values of the relative error, which shifts the mean error away from zero.

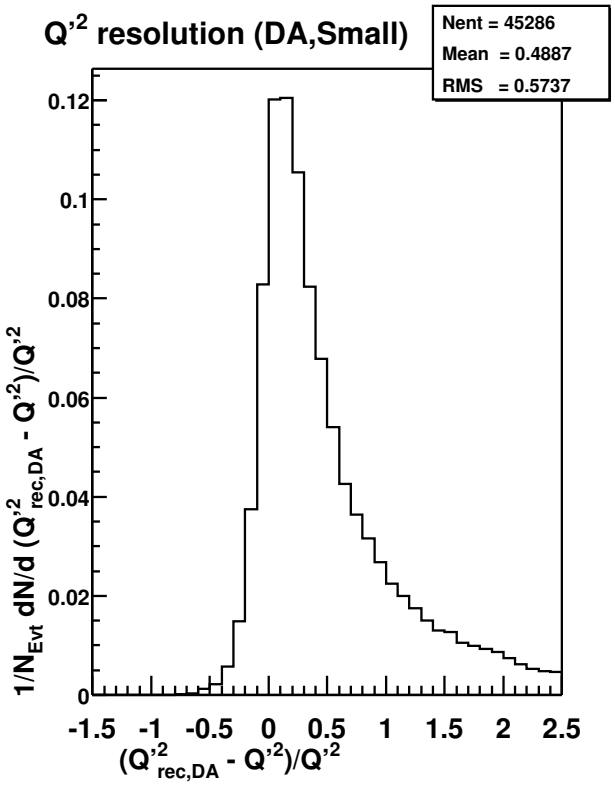

Figure 12: relative error of Q'^2, reconstructed using the DA method and information from the jet with radius $r < 0.7$ (eq. 6). A cut on the p_t of the current jet candidate of $p_t > 4\mathrm{GeV}$ has been applied.

5.6 Comparison of Data and Monte Carlo Simulation

As a check of how well the normal DIS Monte Carlos describe the data, the kinematic quantities Q^2, x_{Bj}, E_e and y_{Bj} have been compared in fig. 13 for data and Monte Carlo.

The histograms in this section include all events that passed the offline cuts (see section 4.3) and the queantities were boosted to the hadronic center of mass frame, where applicable. The same cuts have been applied to all of the Monte Carlos (after reconstruction) and Data.

The normal DIS Monte Carlos agree with the data distribution in Q^2_{DA}, although deviations can be seen at low x_{DA} values and especially in the energy spectrum of the reconstructed electron.

The instanton MC shows significant differences from normal DIS events, especially in the y_{JB} distribution. As it is based on HERWIG as well, initial state radiation is not implemented in QCDINS, but may be incorporated by a user routine.

Fig. 14a) shows the $E - P_z$ distribution. The shape is reproduced by the Monte Carlo programs, although all exceed the data in the region around the maximum, while at low values data exceeds the Monte Carlos.

Fig. 14b) shows the total E_T distribution. The transverse energy E_T^i of an energy deposit cluster in the calorimeter (the basis for zufos) is defined as the transverse component with respect to the $\gamma^* p$-axis of the corresponding zufo's momentum. For all zufos the transverse momentum (at high enough energies, the mass of the objects described is neglected, and their energy is set equal to the magnitude of their momentum) is summed to calculate

$$E_T = \sum_i p_{t,i}$$

where i runs over all zufos and $p_{t,i}$ is the transverse momentum of the ith zufo. HERWIG tends to overestimate the transverse energy at low values, and underestimate it at higher values. The description by Ariadne is considerably better. Simulated instanton induced events are more often at higher values of E_T.

Fig 15a) shows the transverse momentum p_t of the current jet candidate. HERWIG and Ariadne overestimate the number of events with jets with small p_t slightly and underestimate it at higher p_t. QCDINS shows a characteristic difference with respect to normal DIS simulated events and data.

Fig 15b) shows the Energy E of the current jet candidate. Ariadne gives a good description of the data, HERWIG underestimates the distribution slightly at low energies and overestimates it at higher energies. QCDINS shows the same behaviour as HERWIG, but more pronounced.

Other comparisons can be found in fig. 16. on the left are distributions after applying the offline cuts only, on the right the same distributions with the ad-

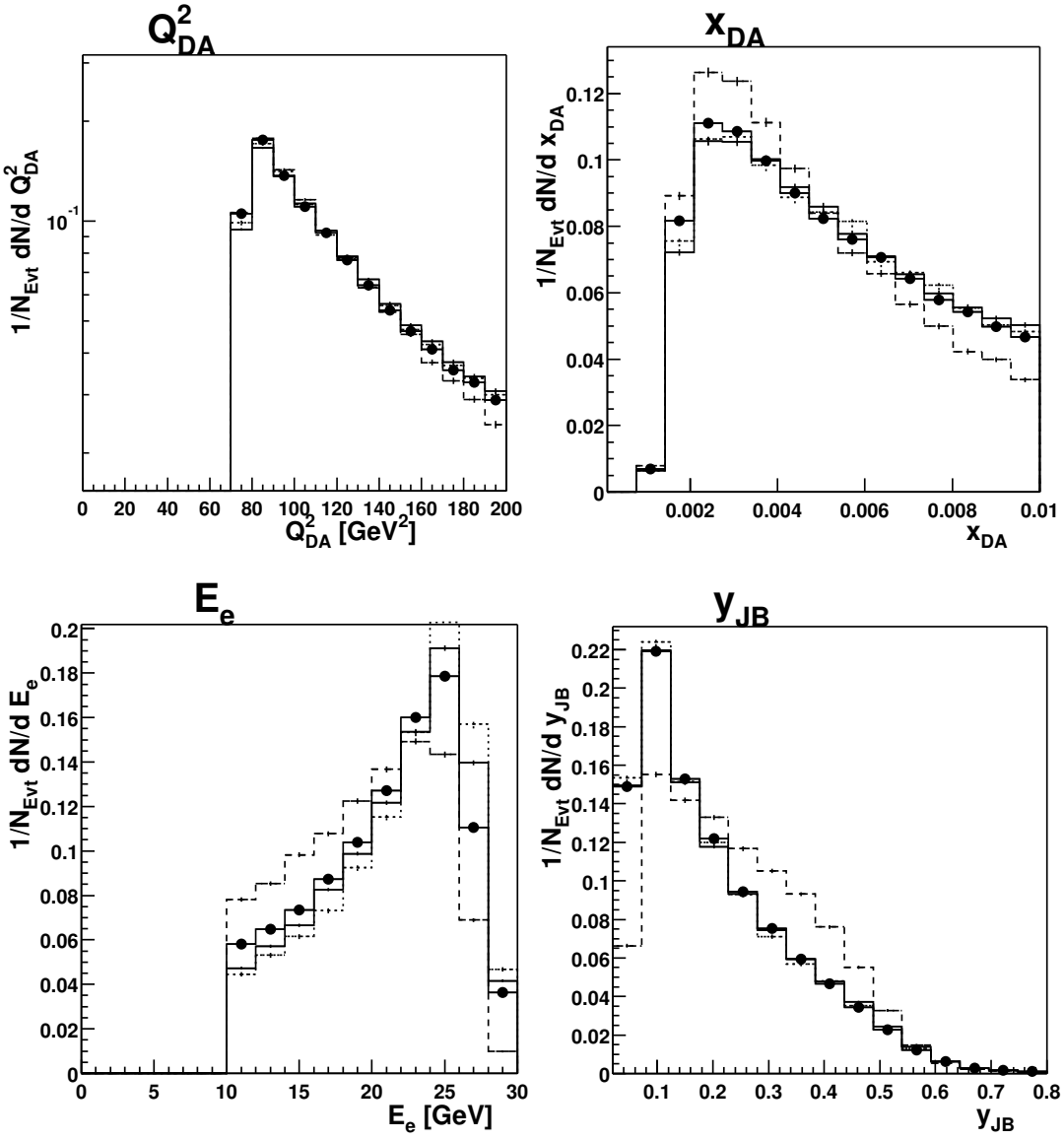

Figure 13: Comparison Data and Monte Carlo: Q^2_{DA}, x_{DA}, E_e and y_{JB} for instanton Monte Carlo (QCDINS), Ariadne, Herwig and Data. All histograms are normalized to the number of events.

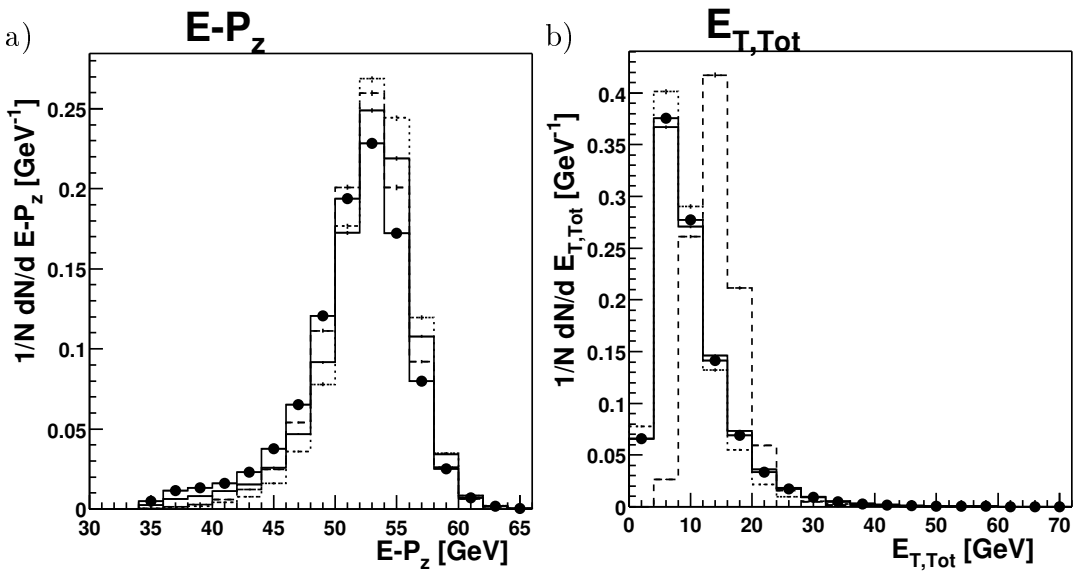

Figure 14: Comparison of Data and Monte Carlo.
a) $E - P_z$ distribution. The shape is reproduced, although all Monte Carlos exceed data in the region around the maximum, while at low values data exceeds the Monte Carlos.
b) Total E_T distribution in the $\gamma^* p$-frame. For all zufos the transverse momentum (the magnitude of the momentum is close to the energy when the energy is high) is summed to calculate E_T. HERWIG tends to overestimate the transverse energy at low values, and underestimate it at higher values. The description by Ariadne is considerably better. Simulated instanton induced events are at higher values of E_T.

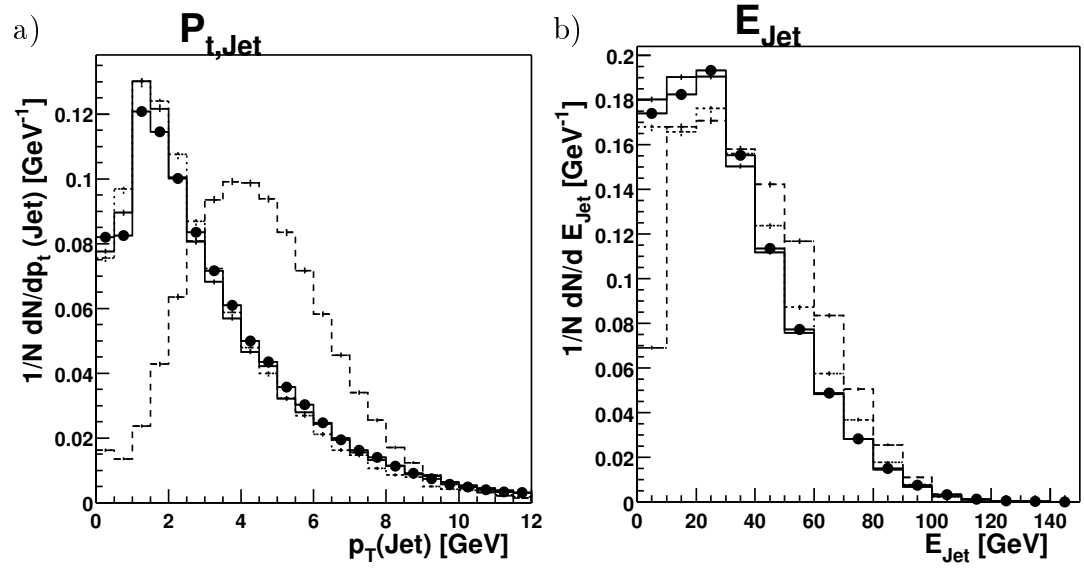

Figure 15: Comparison of Data and Monte Carlo in the $\gamma^* p$-frame.
a) transverse momentum p_t of the current jet candidate. HERWIG and Ariadne overestimate the number of events with jets with small p_t slightly and underestimate it at higher p_t. QCDINS shows a characteristic difference.
b) Energy E of the current jet candidate. Ariadne gives a good description of the data, HERWIG underestimates the distribution slightly at low energies and overestimates it at higher energies. QCDINS shows the same behaviour as HERWIG, but more pronounced.

ditional requirement of exactly two jets that both have a p_t above 4GeV in the hadronic center of mass.

Fig. 16a) shows the total E_T distribution of the event excluding the current jet candidate. For all zufos not assigned to the current jet candidate, the transverse momentum p_t is summed to calculate the total E_T. There is a considerable difference in the mean E_T for instanton induced events and for normal DIS events, which largely disappears in fig. 16b) with the requirement of exactly two jets which both have a transverse momentum larger than 4GeV.

The same can be seen in fig. 16c) (number of tracks passing the quality cuts of section 5.3) and fig. 16d) (number of tracks with the additional requirement of two jets with p_t above 4GeV.

These distributions show that events from the instanton MC look similar to dijet events from a normal DIS MC, when requiring two jets with a transverse momentum above 4GeV in the final state.

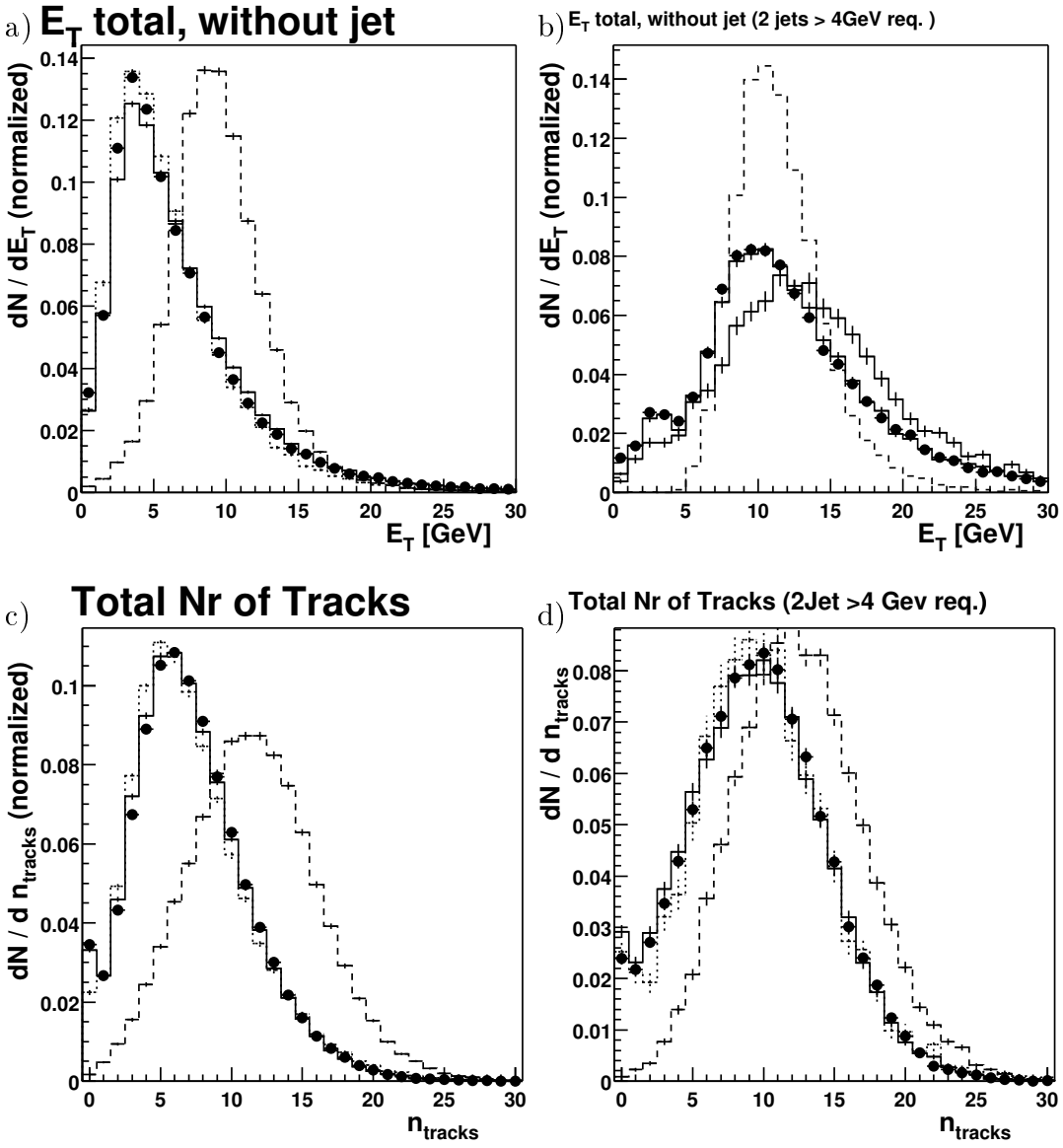

Figure 16: Comparison of Data and Monte Carlo in the $\gamma^* p$-frame.
a) For all zufos i not assigned to the current jet candidate, the transverse energy E_T^i is summed to calculate E_T. [The sum in fig. 14b) runs over all zufos, including the jet]
b) the same distribution with the additional requirement of exactly 2 jets with $p_t > 4$GeV.
c) total number of tracks.
d) total number of tracks for events with 2 jets with $p_t > 4$GeV.

A further comparison is the distribution of $Q'^2_{\rm rec}$, as reconstructed with the double angle variables and the small Jet radius, see fig. 17. The jet used to reconstruct $Q'^2_{\rm rec}$ has been required to have a transverse momentum $p_t > 4$GeV; the histograms are normalized to the number of events in each sample.

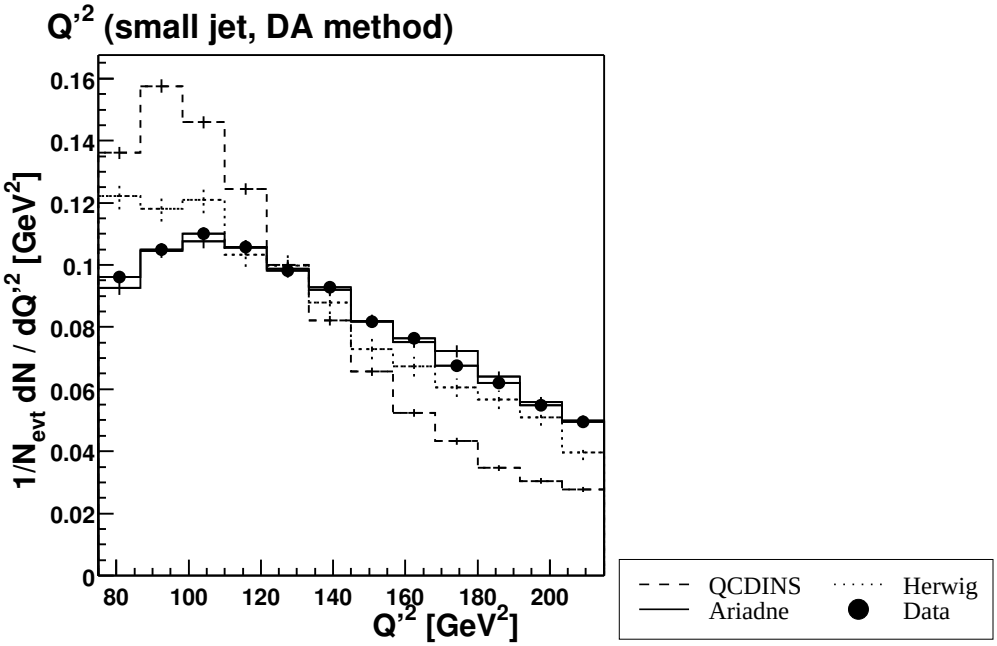

Figure 17: Comparison of $Q'^2_{\rm rec}$. The histograms are normalized to the number of events. Ariadne follows the data points accurately, while HERWIG over- und underestimates the data points at low and high values of $Q'^2_{\rm rec}$, respectively. The difference of the instanton MC and data is still more pronounced, yet following the same trend as HERWIG.

The Ariadne MC follows the data points closely, while HERWIG has too many events at low values of $Q'^2_{\rm rec}$ and not enough at higher values of $Q'^2_{\rm rec}$. The difference of the instanton MC and the data points is still more pronounced, yet following the same trend as HERWIG. The shape of the instanton events is dominated at low Q'^2 by the effect of the generator cuts at $Q'^2 > 64\text{GeV}^2$ and the resolution of the reconstructed Q'^2.

6 Identification of Instanton-induced events

6.1 Comparison of Jet Properties

Instanton induced events tend to have more jets than normal DIS events. To illustrate this, jet multiplicities for various p_t cut-offs have been plotted in fig. 18. To the left is always normal DIS, to the right Instanton induced events.

The cuts applied to the figures in this section are the offline cuts from section 4.3.

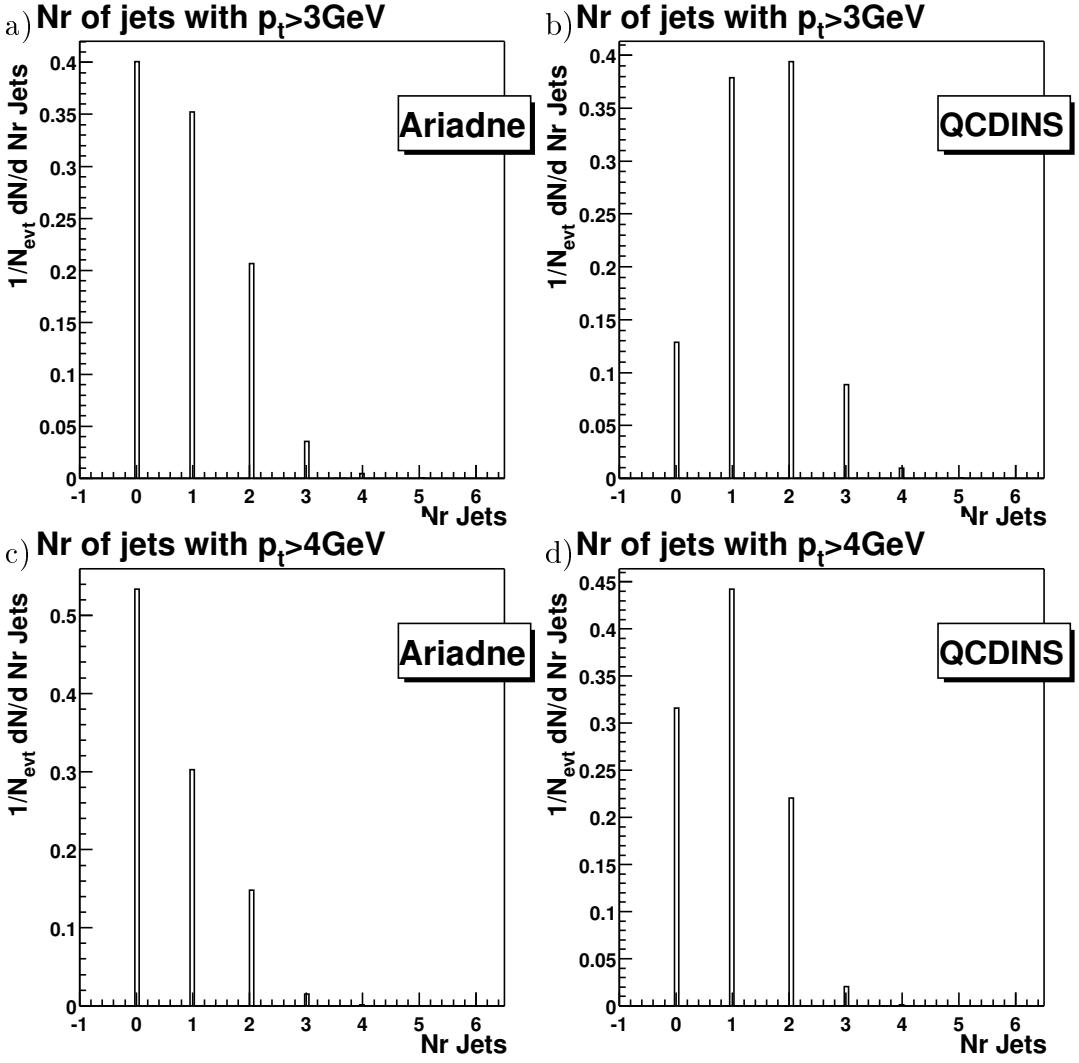

Figure 18: Fraction of events with a given number of events. a) and b) show the jet multiplicity for Ariadne and QCDINS with a jet p_t cut of 3GeV respectively. c) and d) show the jet multiplicity for a jet p_t cut of 4GeV. The instantanton MC has more jets than Ariadne, independent of the jet p_t cut

The top two pictures show the multiplicity distribution for a jet p_t cut of 3 GeV, the lower pictures for a p_t cut of 4 GeV. The instantanton MC has more jets than Ariadne, independent of the jet p_t cut.

6.2 Sphericity

A promising variable that can be used to distinguish normal DIS events from instanton-induced events is the **sphericity** in the instanton-decay quadrant (see below).

Event shape variables such as the sphericity S were originally used in electron-positron annihilation reactions. They are observables that describe the global shape of events.

The sphericity S is calculated as a linear combination of the eigenvalues of the momentum tensor

$$M_{\alpha\beta} = \sum_j p_{j\alpha} p_{j\beta}$$

where $p_{j\alpha}$ is the αth component of the momentum of particle j. The index j runs over all particles for which the sphericity has to be determined and $\alpha = 1, 2, 3$. Sorting the eigenvalues $Q_i, i = 1, 2, 3$ (normalized to the sum of the squares of the particles' momenta $\sum_j \vec{p}_j^{\,2}$) such that $0 \leq Q_1 \leq Q_2 \leq Q_3$, the sphericity S is calculated as:

$$S = \frac{3}{2}(Q_1 + Q_2)$$

A more detailed discussion can be found in [WZ79].

The sphericity S takes on values close to $S = 0$ for very narrow events. For events that have an isotropic structure the sphericity tends to assume values close to $S = 1$. Values of S always lie in the closed interval $[0, 1]$.

When analyzing instanton-induced events, it seems reasonable to divide the zufos into quadrants. The instanton-decay quadrant mentioned above is defined by all zufos i that in the hadronic center of mass frame (HCM) have an azimuthal angle φ_i for which the difference $|\varphi_i - \varphi_{\text{Jet}}|$ to the azimuth angle of the current jet φ_{Jet} is greater than $\pi/2$ (requiring the difference to be mapped into the interval $[-\pi, \pi]$). The remaining zufos are said to belong to the current quadrant and contain the fragmentation products of the current quark. An additional requirement is that the longitudinal momentum $p_{z,i}$ be greater than zero (i.e. in the direction of the virtual photon), to minimize the influence of the proton remnant, thus discarding all zufos assigned to the remaining two quadrants. The decision tree for each zufo is:

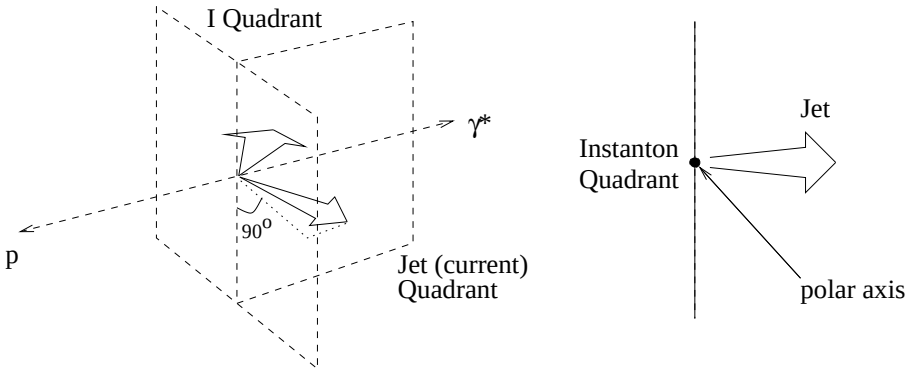

Figure 19: Division of Events in two quadrants by the jet stemming from the current quark. Zufos with longitudinal momentum in the proton direction are discarded, the remaining zufos are assigned according to their azimuth angle with respect to the jet candidate to either the instanton (I,large arrow) quadrant or the quadrant containing the jet (small arrow). To the right is a view in the direction of the virtual photon.

$$
\begin{array}{lcll}
p_{z,i} \leq 0 & \rightarrow & \text{ignore} & \\
p_{z,i} > 0 & \rightarrow & |\varphi_i - \varphi_{\text{Jet}}| \leq \frac{\pi}{2} & \rightarrow \text{ jet quadrant} \\
 & \hookrightarrow & |\varphi_i - \varphi_{\text{Jet}}| > \frac{\pi}{2} & \rightarrow \text{ instanton quadrant}
\end{array}
$$

This division of the events is illustrated in fig. 19. It is motivated by the fact that in order to conserve momentum, the decay products of the instanton subprocess have to balance the jet's transverse momentum stemming from the current quark. The higher the transverse momentum of the jet, the more likely it is that all the instanton decay products are confined to the opposite quadrant.

To compute the sphericity S, the zufos in each quadrant have been boosted to their respective center of mass.

6.2.1 Sphericity resolution

Fig. 20 shows the difference of sphericity at detector level and sphericity at hadron level ($\Delta S = S_{\text{Detector}} - S_{\text{Hadron}}$) for the QCDINS Monte Carlo. At the top of the figure, ΔS is shown for the current quadrant (a) and the instanton quadrant (b), using zufos. In c) and d), the same plots are shown, except that this time tracks have been used to determine the sphericity.

The cuts applied in this and the following figures of this sections are the offline cuts from section 4.3.

The distributions show that the sphericity resolution is slightly better when using zufos, which has been done throughout this analysis.

Fig. 21 shows a direct comparison of the sphericity values at hadron level and

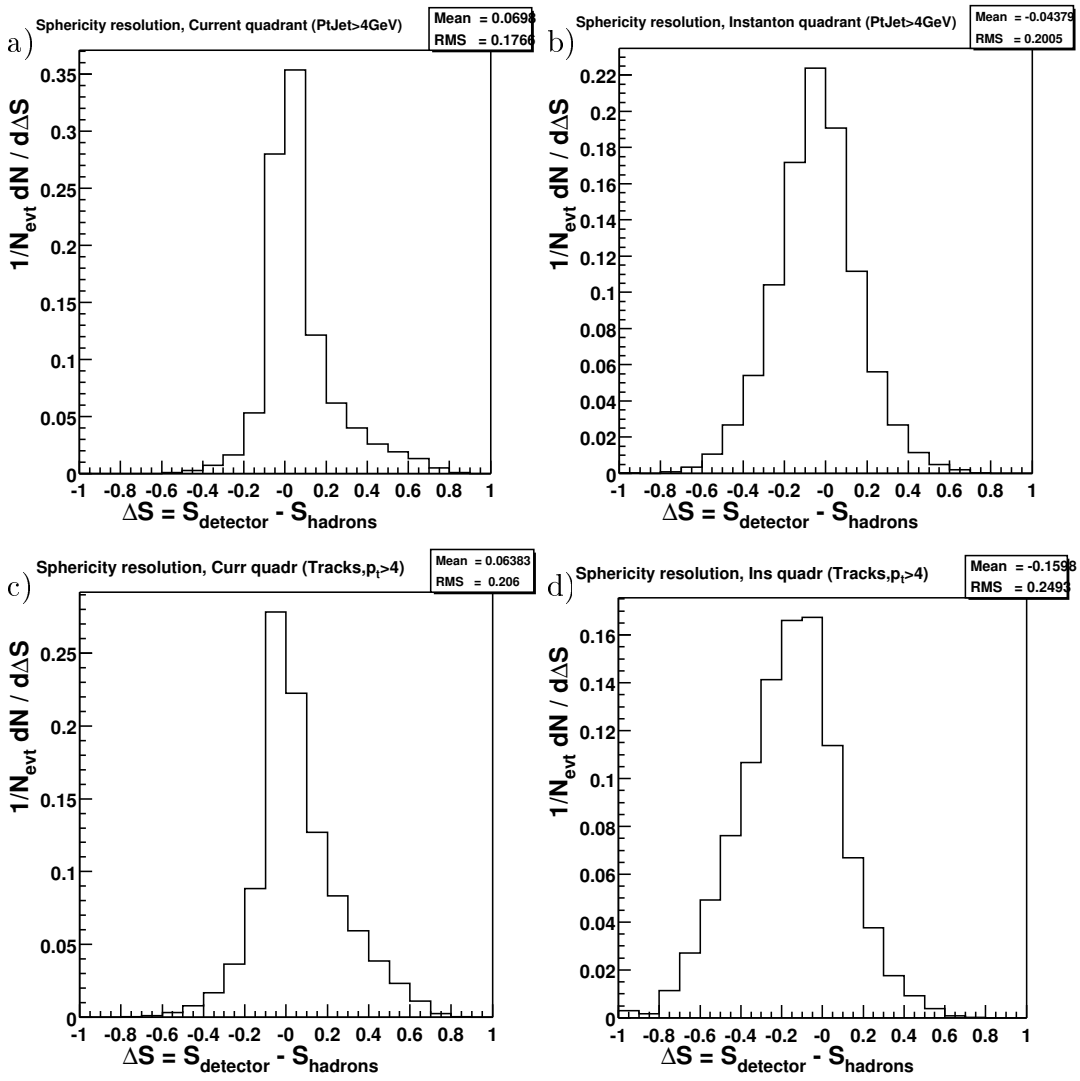

Figure 20: Resolution of the sphericity determination for the instanton Monte Carlo.
a) sphericity at detector level minus sphericity at hadron level (ΔS) in the current quadrant.
b) ΔS in the instanton quadrant.
c) ΔS in the current quadrant, using tracks.
d) ΔS in the instanton quadrant, using tracks.
The sphericity resolution is better when using zufos, which has been done in this analysis.

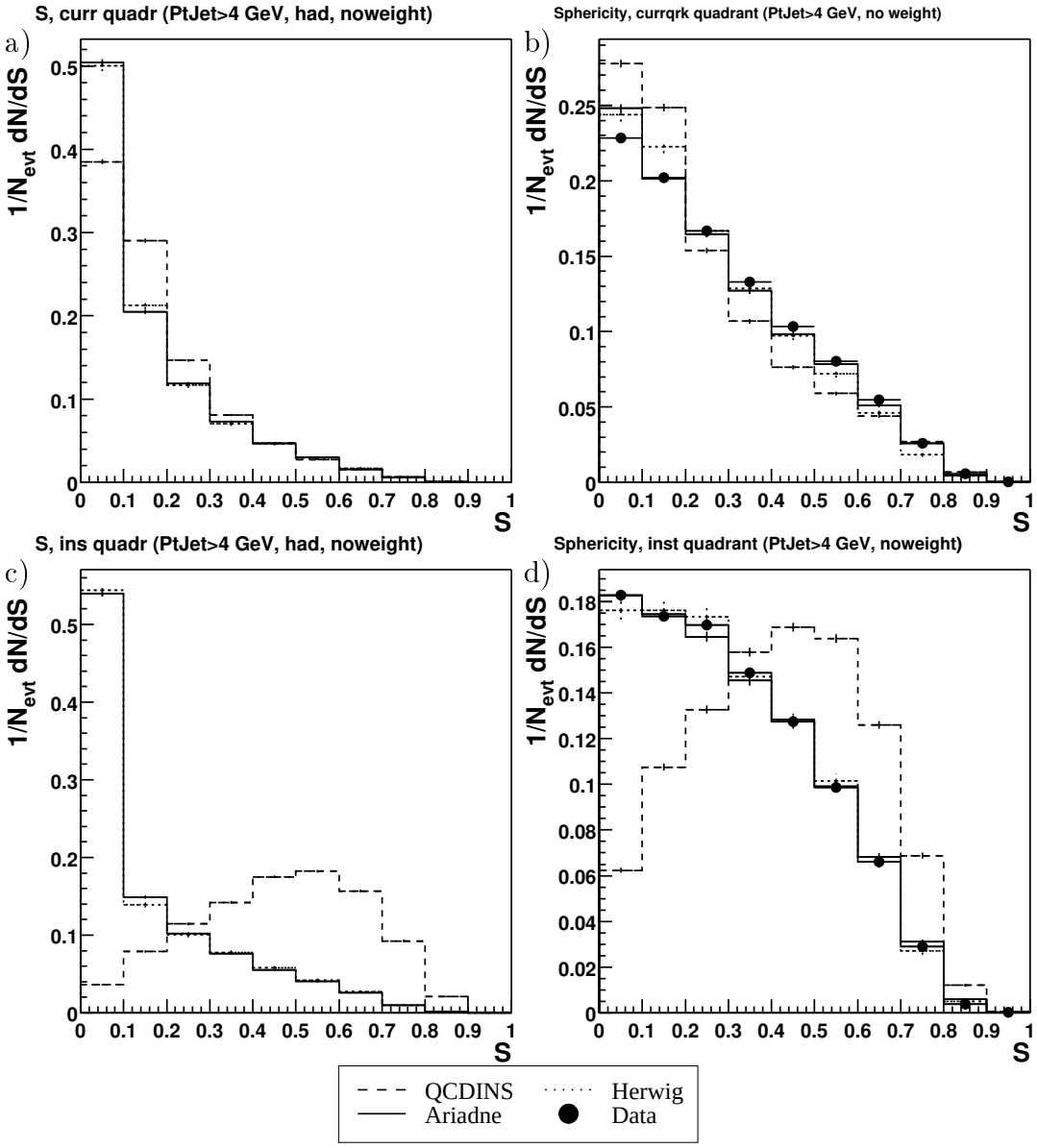

Figure 21: Comparison of Sphericity S at hadron and detector level.
a) S at hadron level in the current quadrant.
b) S at detector level in the current quadrant.
c) S at hadron level in the instanton quadrant.
d) S at detector level in the instanton quadrant.

the reconstructed sphericity S values at detector level.

In figs. 21a) and b) the sphericity S of the current quadrant is shown at hadron level and at the detector level, respectively. In addition to the offline cuts from section 4.3, a jet p_t cut of $p_t > 4\text{GeV}$ has been applied. At hadron level, the agreement between Ariadne and HERWIG is very good, the instanton Monte Carlo has roughly the same shape but disagrees in the region $S < 0.3$. It is possible that some zufos belonging to the instanton decay are assigned to the jet quadrant and influence the sphericity computation. The difference between instanton and normal DIS MC lessens at detector level, due to resolution effects.

In figs. 21c) and d) the sphericity S of the instanton quadrant is shown at hadron level and at the detector level, with a jet p_t cut of $p_t > 4\text{GeV}$. There is almost perfect agreement between the normal DIS MCs at hadron level in the instanton quadrant, and a significant difference from the instanton MC. The distributions for normal DIS and instanton MC approach each other at detector level due to the sphericity resolution, but still remain distinct.

6.2.2 Comparison of Sphericity QCDINS - normal DIS

In fig 21b) the sphericity distribution of the current quark quadrant is shown. The dominant process in this quadrant for the instanton Monte Carlo is the hadronization of the current quark, which is what is expected in normal DIS events as well. Since the fragmentation of a single quark should be decribed in the same manner for a normal DIS Monte Carlo and for an instanton Monte Carlo, the sphericity distribution in this quadrant should look the same for both normal DIS and instanton Monte Carlo and can be used as an agreement check.

Except at very low values of S, Ariadne agrees well with the data points, while HERWIG is more likely to show small disagreements. The difference between instanton Monte Carlo and data is more prominent, which might be a consequence of decay products of the instanton process that reach the jet quadrant.

Fig. 21d) shows the distributions of the Sphericity in the instanton quadrant. Again, the description of the data points by Ariadne and HERWIG is satisfying, whereas the instanton MC shows a significantly different shape. This can be expected, because the instanton decay products decay isotropically in the rest frame of the instanton process, which we are examining. The sphericity of the instanton quadrant will be used to determine a limit to the instanton fraction found in the data.

Furthermore, the Sphericity distributions are plotted in fig. 22 with a cut of $Q'^2 > 75\text{GeV}^2$ and with the requirement of exactly two jets in the HCM with a $p_t > 4\text{GeV}$.

It can be seen from these plots that although instanton induced events tend to look similar to two jet DIS events, the sphericity still can be used to discriminate between the two.

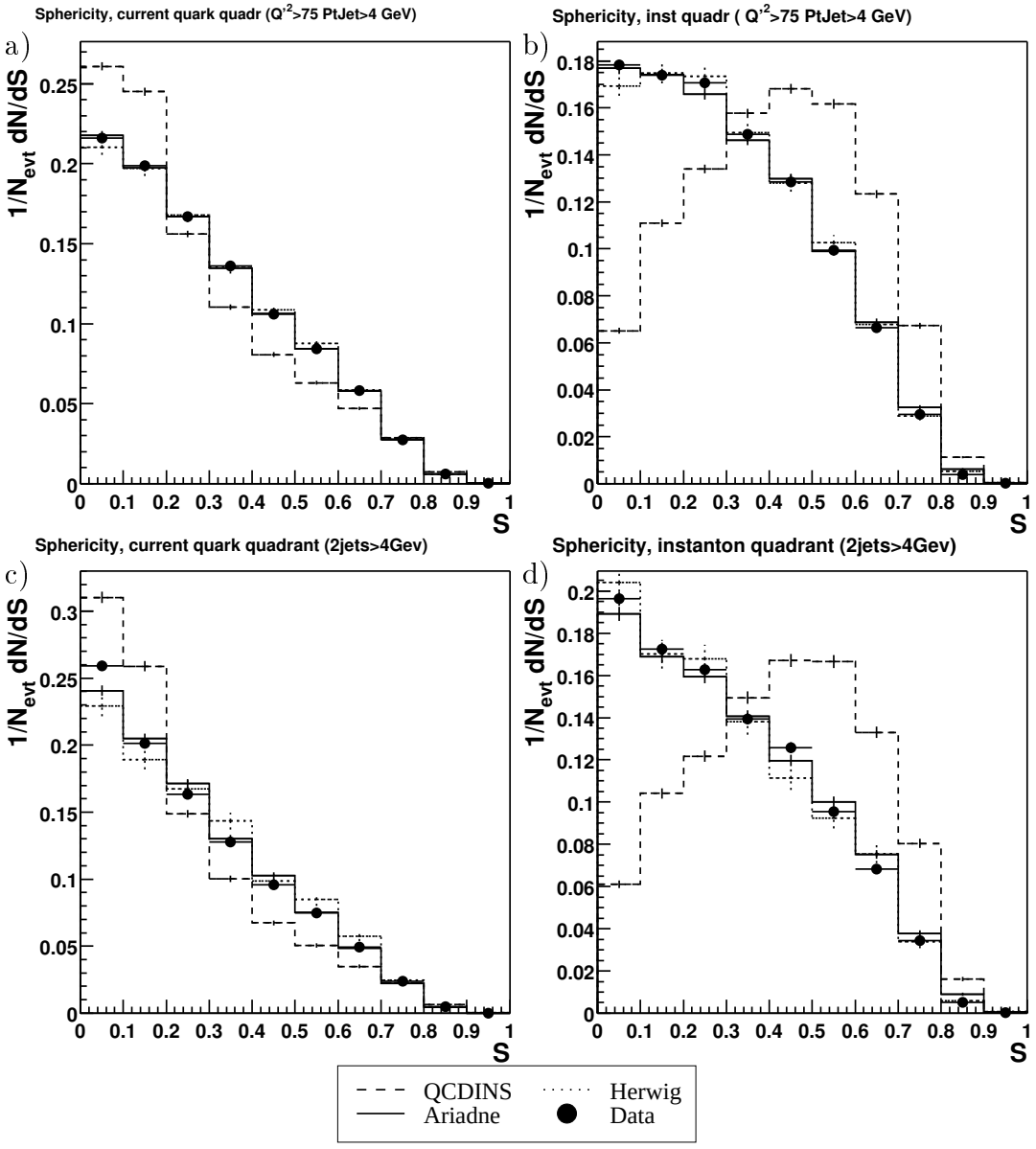

Figure 22: a) sphericity of jet quadrant with the requirements $Q'^2 > 75\mathrm{GeV}^2$, $p_{t,\mathrm{Jet}} > 4\mathrm{GeV}$
b) sphericity of instanton quadrant with $Q'^2 > 75\mathrm{GeV}^2$, $p_{t,\mathrm{Jet}} > 4\mathrm{GeV}$
c) sphericity of jet quadrant with the requirement of exactly two jets with $p_t > 4\mathrm{GeV}$.
c) sphericity of instanton quadrant with the requirement of exactly two jets with $p_t > 4\mathrm{GeV}$.

6.3 Enhancement of the Instanton fraction (final cuts)

As a step to improve the limit on the instanton contribution, we will enrich the fraction of possibly instanton-induced events in the final sample. To do so, regions in the space spanned by several observables that have a higher density of instanton-induced events than of normal DIS events will be selected.

The variables considered in this search stem exclusively from the instanton quadrant defined above. They are:

- **Energy** E: The total energy of the zufos in the instanton quadrant.
- **transverse Energy** E_t: The sum of the transverse momenta of the zufos in the instanton quadrant.
- **Mass** M: The mass $M = \sqrt{(\sum_i E_i)^2 - \sum_{j=x,y,z}(\sum_i p_{j,i})^2}$ of the system of the zufos, where both indices i run over all zufos in the instanton quadrant and E_i is the energy of zufo i, and $p_{j,i}$ its momentum along axis $j = x, y, z$.
- **multiplicity** n: The number of tracks in the instanton quadrant. (The requirements for tracks are defined in section 5.3).
- **Sphericity** S: The sphericity calculated from the zufos in the instanton quadrant.

The sphericity seems to be only weakly correlated with the other observables. This can be seen for example in fig. 23, where the Mass M has been plotted against the Sphericity S.

Most of the other variables show stronger correlations. Figure 24 shows two-dimensional plots of E_t/M and E_t/E for QCDINS and Ariadne, respectively. The strong correlation between E_t and M (E_t and E) for instanton Monte Carlo can be seen in fig. 24a) and b). Most events from the instanton MC are in a region above an E_t of 5GeV.

In fig. 24c) and d) the correlation between E_t and M (E_t and E) for Ariadne can be seen. Most events from Ariadne cluster at low values of E_t.

The plots show a possibility to enhance the instanton fraction by applying cuts in E_t, E or M. It can be seen that most normal DIS events cluster at low values of E and E_t.

Fig. 25a) shows the ratio of the event density in E_t and M bins of instanton MC over Ariadne. Only those regions are shown, where both the instanton MC and Ariadne have more than 20 events, to minimize statistical fluctuations.

Fig. 25b) additionally requires that the ratio of the densities be greater than 2. Using this information, an area has been defined, which determines the events to be selected. The area is illustrated in fig. 25b) and corresponds to a logical AND of the following requirements:

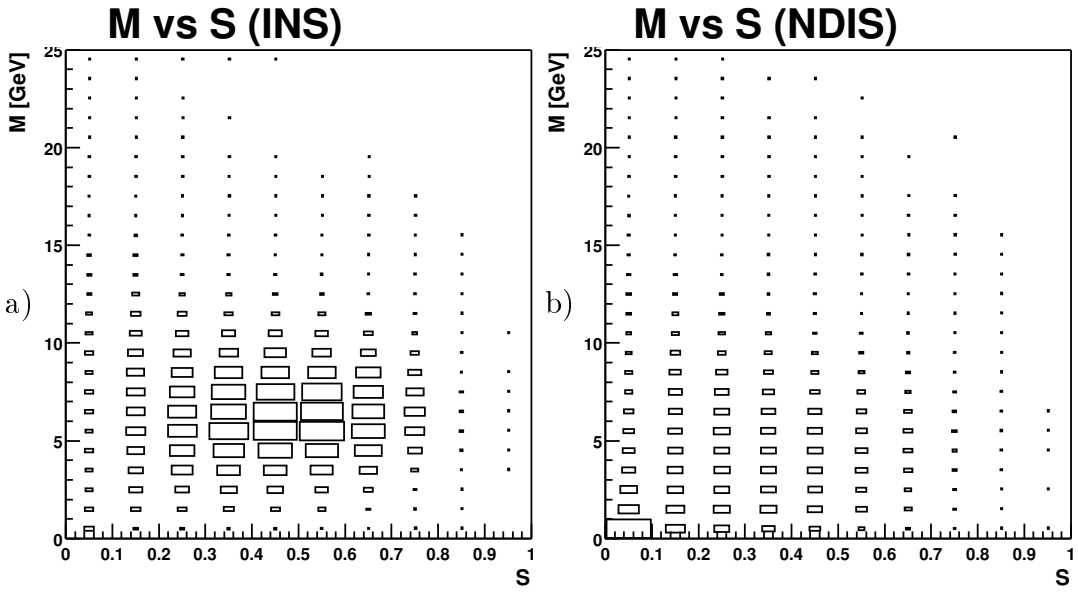

Figure 23: Mass M vs Sphericity S. a) QCDINS, b) Ariadne.

- $5\text{GeV} < E_t < 12\text{GeV}$
- $5\text{GeV} < M < 12\text{GeV}$
- $E_t < M + 2\text{GeV}$
- $E_t > M - 2\text{GeV}$

Due to the strong correlation between E, E_t, M and n the additional cuts will be restricted to E_t and M.

Final Cuts:

The final cuts are:

- $P_{t,Jet} > 4\text{GeV}$
- $Q'^2 > 75\ \text{GeV}^2$: Apart from allowing a further reduction of normal DIS event "contamination", this cut is applied to account for the fact that normal DIS events are allowed to assume all possible values of Q'^2, while in QCDINS, they were cut off at $Q'^2 > 64\text{GeV}^2$
- $n > 5$: (number of tracks in the instanton quadrant) this cut is applied to allow for a reliable S calculation in addition to further decreasing the fraction of normal DIS events.
- E_t and M: See fig. 25b) for the area selected in E_t and M

In the following, 'final cuts' will always refer to these cuts.

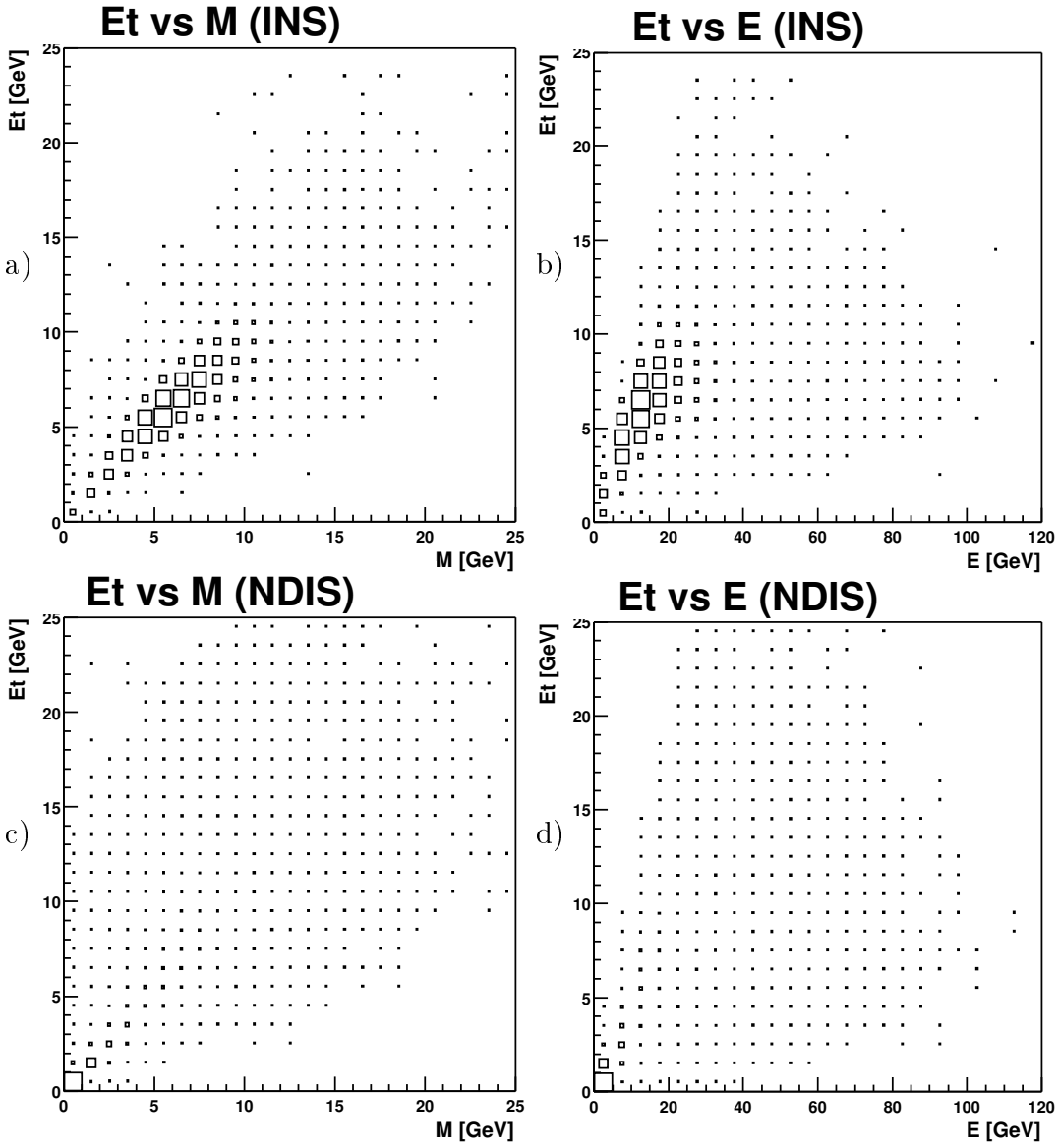

Figure 24: Correlations of E_t/M, E_t/E.
a) E_t/M, instanton MC
b) E_t/E, instanton MC
c) E_t/M, Ariadne
d) E_t/E, Ariadne

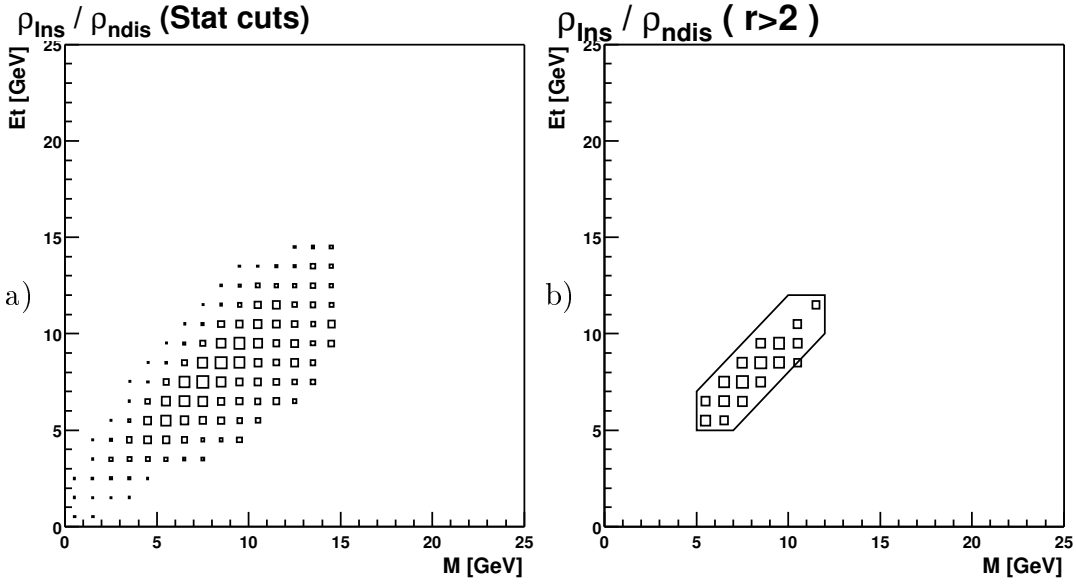

Figure 25: Et Vs M, QCDINS density divided by normal DIS density.
a) Only bins with more than 20 events are considered.
b) Additionally, the instanton density is required to be twice the normal DIS event density. The lines denote the region defined by the cuts.

6.4 Variation of QCDINS parameters

To estimate the dependence of the sphericity on the central parameters of the instanton process, we have varied the central parameters of QCDINS: x' and Q'^2.

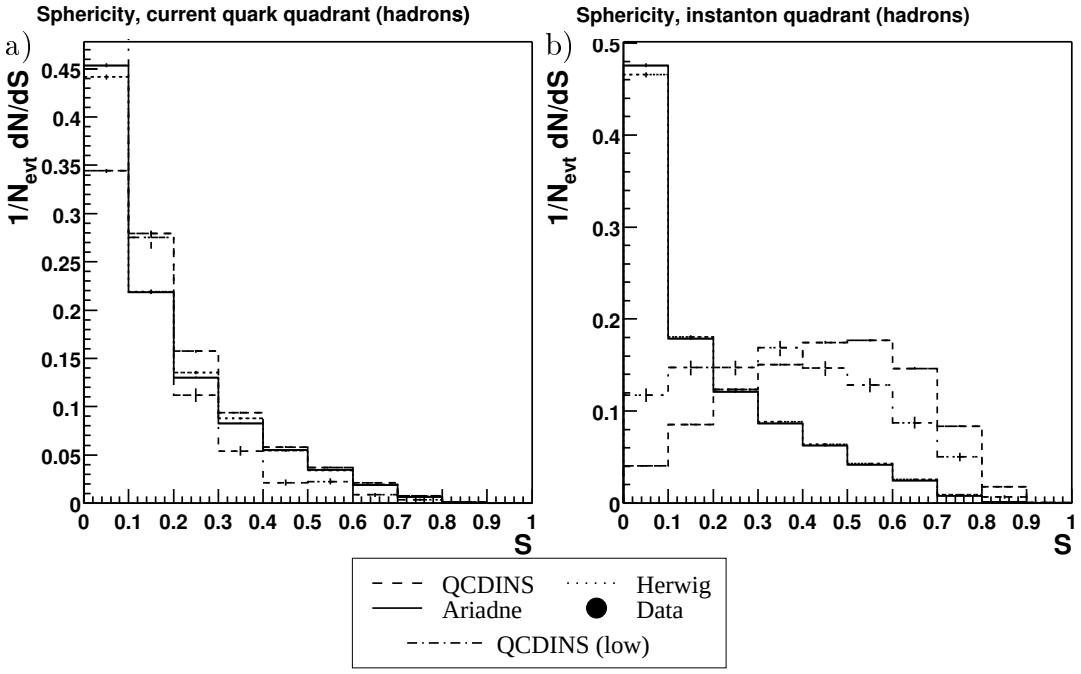

Figure 26: QCDINS(low) refers to a set of Instanton MC events with generation cut of $x' > 0.25$ and $Q'^2 > 16GeV$
a) sphericity in the current jet quadrant
b) sphericity in the instanton quadrant

Figure 26 shows a comparison of normal DIS Monte Carlos and Instanton Monte Carlo at nominal parameters ($x' > 0.35$, $Q'^2 > 64GeV$) and instanton MC at low parameters values: $x' > 0.25$ and $Q'^2 > 16GeV$. It can be seen that the Sphericity distribution in the instanton quadrant is shifted to lower values by decreasing x' and Q', while still maintining a shape different from normal DIS. The consequences are that if a significant fraction of instanton induced events have a small Q'^2, they will be harder to distinguish from normal DIS events.

Fig. 27 shows the p_t spectrum of the current jet candidate in the HCM frame. It can be seen, that for low values of x' and Q'^2, the p_t spectrum of the jet candidate is shifted towards lower values.

Therefore, cutting at a jet p_t of 4 GeV, we isolate those instanton-induced events that have a higher sphericity in the instanton quadrant, and stem from the confidence region of the QCDINS MC. This will make results more directly comparable to theoretical predictions and assures a better distinction between normal DIS

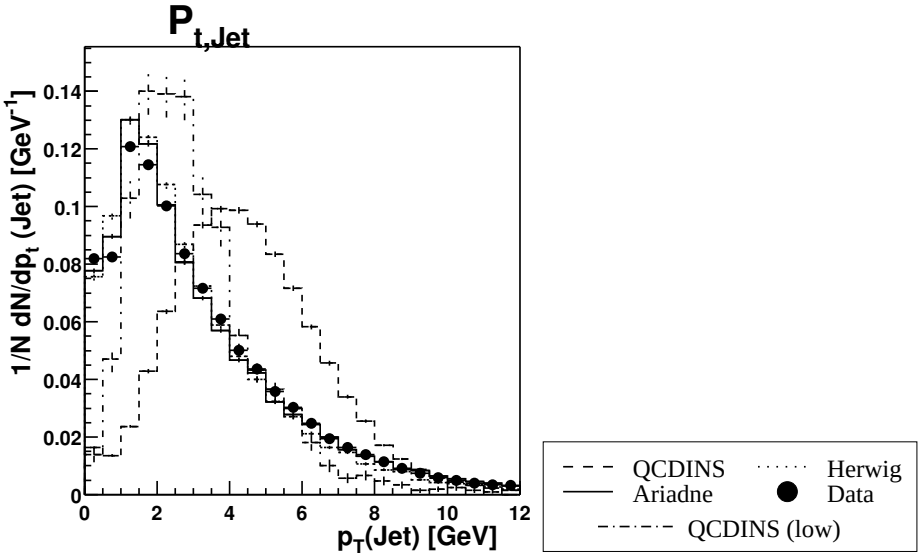

Figure 27: p_t spectrum of the current jet candidate in the hadronic center of mass frame. The instanton MC generated at $x' > 0.25$ and $Q'^2 > 16\mathrm{GeV}^2$, QCDINS(low), shows a p_t distribution very close to normal DIS MC and data.

and instanton events in the sphericity.

This effect is shown directly if fig.28. Cutting on the transverse energy of the jet in the HCM significantly reduces the number of events generated with a low value of x' and Q'^2, but retains the characteristic shape of the x' distribution.

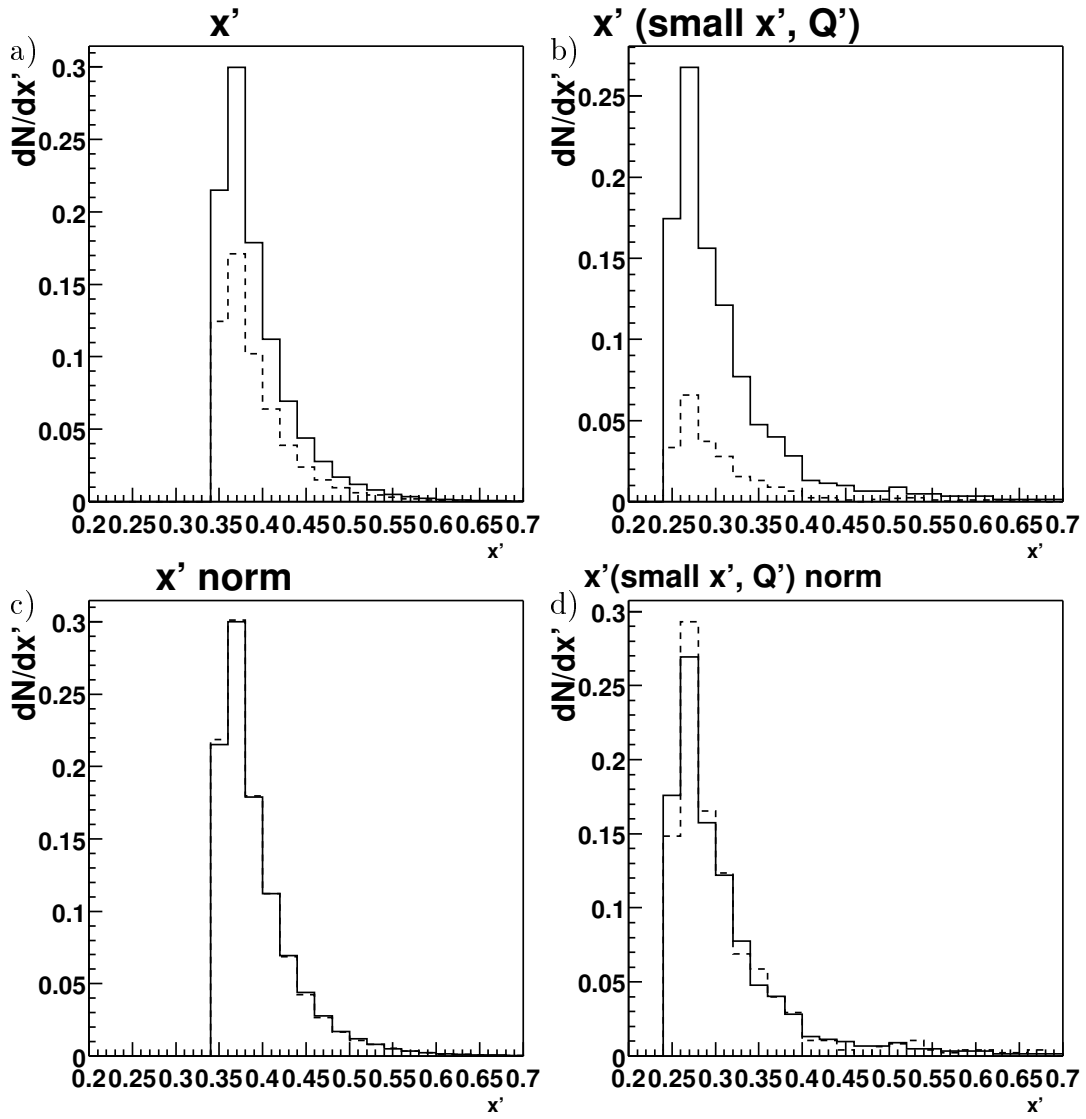

Figure 28: a) x' spectrum for instanton MC at nominal values without jet p_t cut (solid line) and with jet $p_t > 4\mathrm{GeV}$ (dashed line).
b) x' spectrum for instanton MC at $x' > 0.25$ and $Q'^2 > 16\mathrm{GeV}^2$ without jet p_t cut (solid line) and with jet $p_t > 4\mathrm{GeV}$ (dashed line).
c) the same as a), with area normalized histograms
d) the same as b), with area normalized histograms
Applying a jet p_t cut reduces the events generated at low values of x' and Q'^2 stronger than at nominal values, while retaining the shape of the distribution.

6.5 K^0_S multiplicity

It has been suggested e.g. in [CGRS99a] to make use of an excess of produced strange particles.

But it turns out, that after applying the final cuts to increase the fraction of instanton induced events, the K^0_S production (at least with the version 1.60.1 of QCDINS) is comparable to that of normal DIS event generators, as shown in table 2.

Generator	fraction of events with $n = 0, 1, 2, 3$ K^0_S			
	0	1	2	3
QCDINS	74%	23%	3%	0.28%
ARIADNE	78%	20%	2.2%	0.37%
HERWIG	74%	23%	2.4%	0.37%

Table 2: Fraction of events with $n = 0, 1, 2, 3$ K^0_S of QCDINS, Ariadne and HERWIG after applying the final cuts

The multiplicities in this table are determined in the instanton quadrant and may be different in other regions.

The table suggests that there is no marked excess of events with K^0_Ss for instanton induced events.

A similar trend has been observed in [CGRS99b], fig. 7b, where it can be seen that K^0 multiplicities are higher for instanton induced events at low particle multiplicities and higher for normal DIS events at higher particle multiplicities (the particles are counted in the 'instanton band', defined in the reference).

It was therefore been decided not to make use of K^0_S identification in this analysis.

6.6 Q'^2 distribution

The difference in shape of the reconstructed Q'^2_{rec} between the instanton MC and normal DIS Monte Carlos (fig. 17, p. 40) becomes even more pronounced, when the final cuts, as described in section 6.3, are applied. This case is shown in fig. 29.

The importance of this figure lies in a way of proving the existence of instantons, once a signal can be found in the data: If the cut on the reconstructed Q'^2 is set to higher values, the effect should disappear. In addition to the final state features that are being used in this kind of analyses, the dependence on Q'^2 (and on x') has to be demonstrated in a signal, as it derives directly from the matrix element.

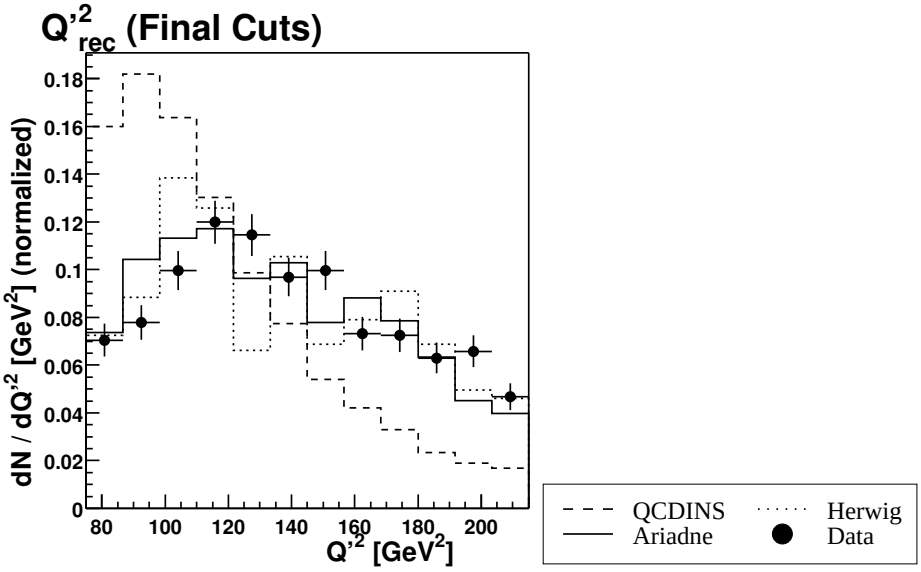

Figure 29: Comparison of Q'^2_{rec} with final cuts.

7 Limit on the instanton cross-section

7.1 Reweighting

The simulation of normal DIS events is not perfect, although ARIADNE gives a good description of the hadronic final state. To improve the description, the simulated normal DIS events have been reweighted.

The distribution used to determine the weights for the individual events is the sphericity distribution in the current quadrant. The distribution of the sphericity for data is divided by the distribution for the Monte Carlo, resulting in a correction factor for each bin.

The result can be seen in fig. 30. To the left, the weights for the Ariadne Monte Carlo can be seen, to the right, the values for the HERWIG Monte Carlo are shown. The lines correspond to a deviation of 5%. It can be seen from these distributions, that the Ariadne Monte Carlo gives a good description of the data, while the correction factors for HERWIG are greater in magnitude.

The results of the reweighting can be seen in fig. 31. In a) and b), the unweighted and reweighted distributions in the current quadrant are shown, respectively. In c) and d), the unweighted (left) and reweighted (right) distributions for the instanton quadrant are shown. The offline cuts were applied, in a addition to the requirement of a current jet candidate with a $p_t > 4$GeV.

Fig. 32 show the sphericity distributions after both reweighting and applying the final cuts. The distributions of fig. 32b) where used for the fits.

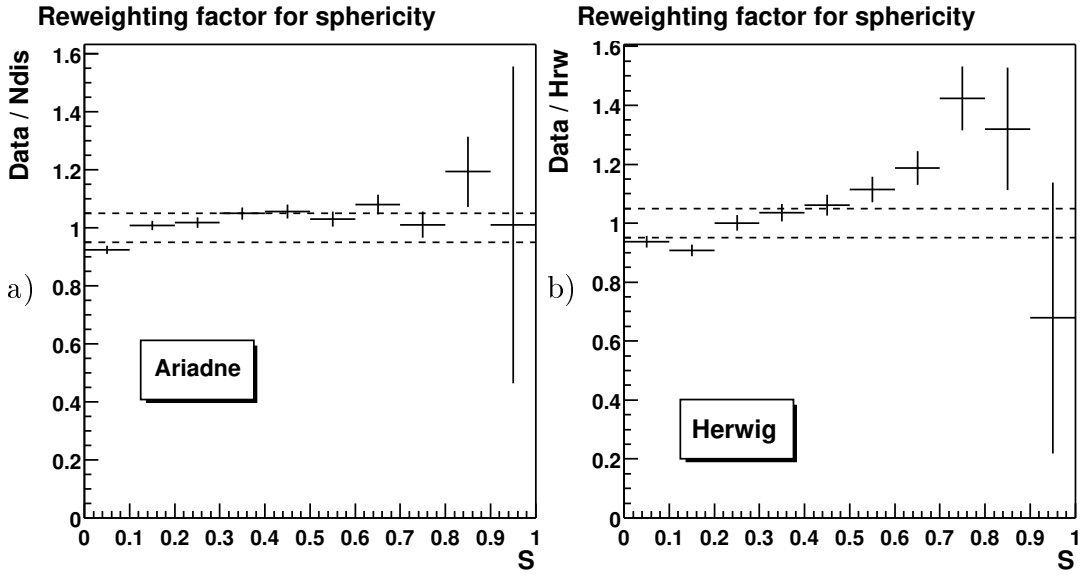

Figure 30: Weights from Sphericity distributions. a) Ariadne, b) HERWIG. Dotted lines correspond to a deviation of 5%.

7.2 Limits from fits to the sphericity distributions

A limit on the cross-section for instanton-induced events can be found by comparing the shapes of the sphericity distribution for simulated instanton and normal DIS events with the data.

The sphericity distributions used for this are from the instanton MC, Ariadne and HERWIG, which are compared to the 1997 data. The cuts applied before comparing the distributions are the final cuts.

The starting point are the number of events n_{iN}, n_{iD}, n_{iI} (i denoting the bin number of sphericity bins, N, D, I denoting NDIS, Data, QCDINS, respectively). The respective errors are $\sigma_{i[N,D,I]} = \sqrt{n_{i[N,D,I]}}$.

Normalizing the histograms by the number of entries $N = \sum_i n_i$, we obtain the distributions $n^*_{i[N,D,I]} = \frac{1}{N_{[N,D,I]}} n_{i[N,D,I]}$ with errors $\sigma^*_{i[N,D,I]} = \frac{1}{N_{[N,D,I]}} \sqrt{n_{i[N,D,I]}}$.

For any fraction f of instanton events we can compute the variable χ^2:

$$\chi^2 = \sum_{i=1}^{k} \frac{\{n^*_{iD} - [f \cdot n^*_{iI} + (1-f) \cdot n^*_{iN}]\}^2}{\sigma^{*2}_{iD} + f^2 \sigma^{*2}_{iI} + (1-f)^2 \sigma^{*2}_{iN}}$$

where k denotes the number of histogram bins with a number of entries greater than 10.

Fig. 33a) shows the χ^2 of the fit as a function of the instanton fraction f. The dashed horizontal line corresponds to the 5% confidence level value of χ^2 and its intersection with the χ^2 curve is used to determine the limiting fraction $f_{\rm lim}$.

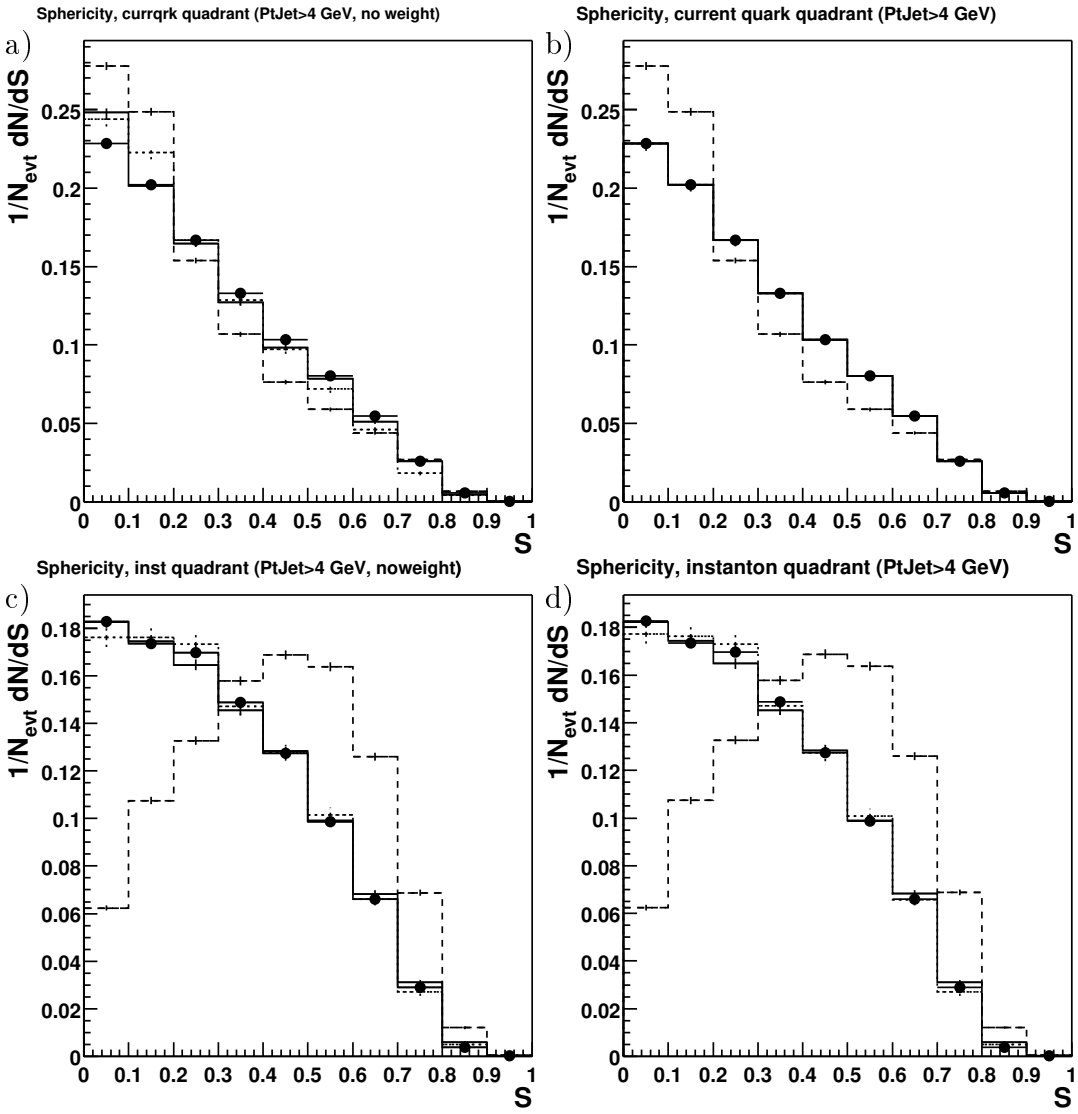

Figure 31: Result of the Weighting procedure.
a) Current quadrant distribution, unweighted and b) weighted. This quadrant was used to determine the weights.
c) Instanton quadrant, unweighted and d) weighted.

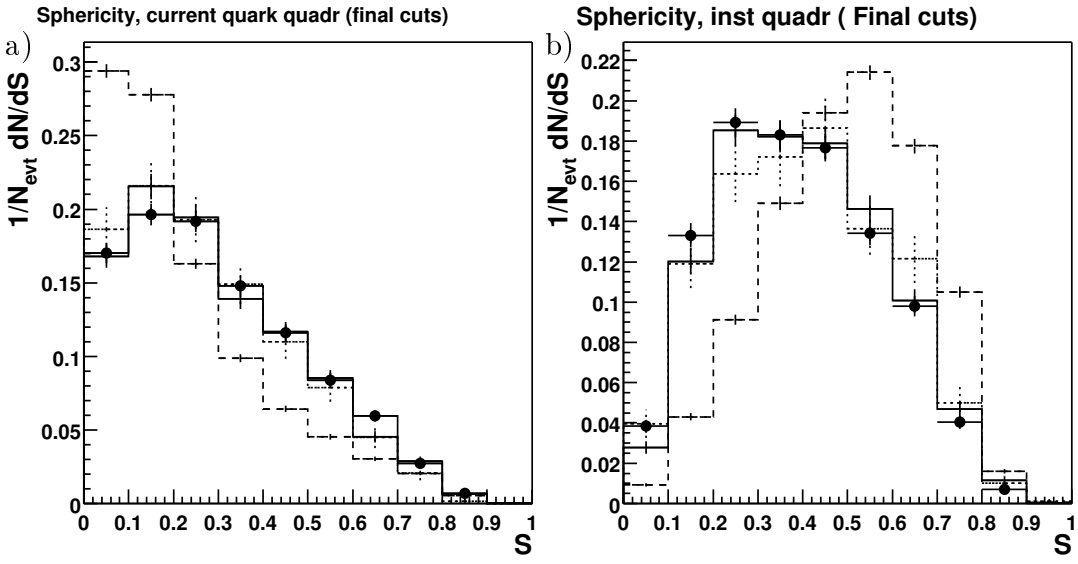

Figure 32: Result of the Weighting procedure after final cuts.
a) Sphericity in the current quadrant distribution and b) in the Instanton quadrant

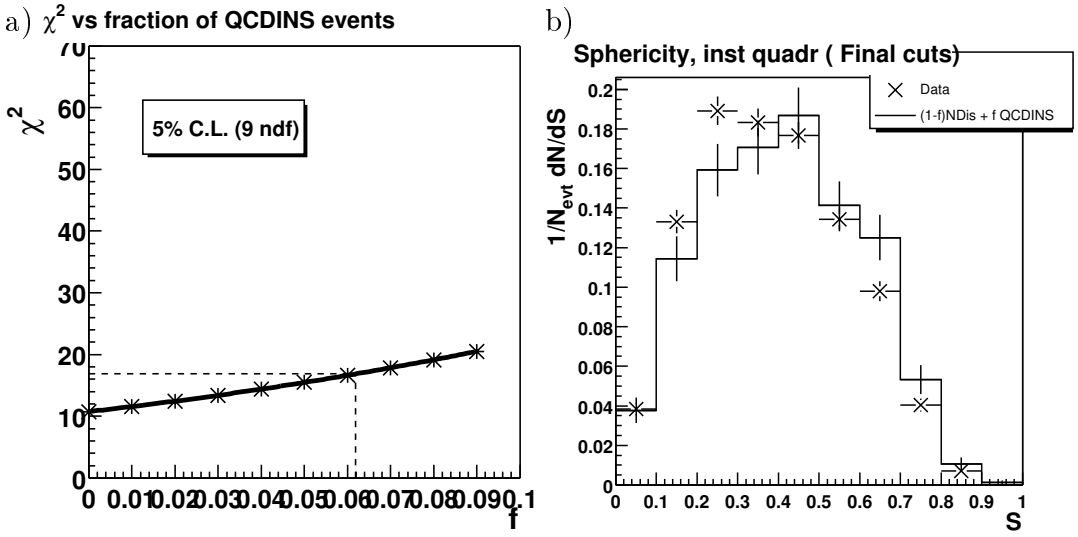

Figure 33: a) χ^2 for nine degrees of freedom vs fraction f: the dashed line indicates the value for f for which the probability of obtaining a corresponding value of χ^2 as high or higher is below 5%.
b) sphericity distribution of a mixture of Ariadne and instanton MC at the fraction $f_{\rm lim} = 0.06$ compared to data points.

The limiting fraction obtained in this way (using Herwig) is

$$f_{\text{lim}} = 0.062$$

A limit using Ariadne has only been obtained using the method of the next section, because the χ^2 is too large even for an instanton fraction of $f = 0$.

7.3 Limit via likelihood ratio

In addition to the direct determination of a limit via the method used in the previous section, a likelihood ratio method can be applied to determine limits[Bra74]. For a probability density f_p that depends on a parameter λ, the likelihood function can be computed for different values of λ. The likelihood ratio Q is then

$$Q = \frac{L_1}{L_2}$$

where L_1 is the value of the likelihood function for parameter $\lambda = \lambda_1$ and L_2 is the value of the likelihood function for $\lambda = \lambda_2$. It is then said that it is Q times more probable that the data are described by a distribution with parameter λ_1 than by a distribution with parameter λ_2.

In the following, the probability density is the sphericity distribution measured for normal DIS MC (Ariadne, HERWIG) with varying contributions of instanton MC. As parameter λ, the fraction f of instanton induced events is introduced. For different values of f, the χ^2 of the sphericity distribution in data is computed, along with the probability P_f of obtaining the value of P_f measured or higher. The likelihood ratio is then formed by these probabilities and the 5% confidence level is determined by the equation

$$\frac{P_{f=0}}{P_{f=f_{\text{lim}}}} = 20$$

where $P_{f=0}$ is the probability in the case of no instanton contribution.

For the final cuts, the limiting fraction determined by the likelihood ratio $f_{\text{lim},LR}$ using Ariadne is

$$f_{\text{lim},LR} = 5.1\%$$

Using HERWIG, the limit is:

$$f_{\text{lim},LR} = 9.1\%$$

Herwig

Cuts	$P(\chi^2)$ (f=0)	χ^2 Limit	LR Limit
curr Jet>4GeV	0.5	0.049	0.055
Jet,Q' >75	0.45	0.036	0.044
Jet,Q' > 100	0.59	0.051	0.057
Jet,Q' >75,$n > 5$	0.11	0.075	0.15
2 Jets>4GeV	0.24	0.086	0.11
Final Cuts	0.29	0.062	0.091

Ariadne

Cuts	$P(\chi^2)$ (f=0)	χ^2 Limit	LR Limit
curr Jet>4GeV	0.0031	(0.0)	0.017
Jet,Q' >75	0.0019	(0.0)	0.018
Jet,Q' > 100	0.0045	(0.0)	0.026
Jet,Q' >75,$n > 5$	2.3e-07	(0.0)	0.034
2 Jets>4GeV	4.5e-05	(0.0)	0.016
Final Cuts	0.057	0.0022	0.051

Table 3: 95% confidence limits for the instanton fraction f from the fits to the sphericity distribution.
For different set of cuts, the following values are given in columns:
• the cuts used
• the probability of the χ^2 for an instanton fraction of 0% ($P(\chi^2)$ ($f = 0$))
• the 5% limit extracted from a fit of the sphericity distributions after the cuts
• the limit determined by the likelihood ratio method

The cuts mentioned correspond to:
• **curr Jet**> 4**GeV:** a current jet candidate with $p_t > 4$GeV
• **Jet,** $Q'^2 > 75$**:** a current jet candidate with $p_t > 4$GeV, $Q'^2 > 75\mathrm{GeV}^2$
• **Jet,** $Q'^2 > 100$**:** a current jet candidate with $p_t > 4$GeV, $Q'^2 > 100\mathrm{GeV}^2$
• **Jet,** $Q'^2 > 75$**,** $n > 5$**:** a current jet candidate with $p_t > 4$GeV, $Q'^2 > 75\mathrm{GeV}^2$, number of tracks in instanton quadrant $n > 5$.
• **2 Jets**> 4**GeV:** two jets with $p_t > 4$GeV
• **Final Cuts:** the final cuts.

7.4 Summary of limits determined using sphericity

The limits calculated from fits to the sphericity distributions can be found in table 3 for Herwig and Ariadne.
For different set of cuts, the following are stated in columns:

- the cuts used
- the probability of the χ^2 at an instanton fraction of 0% ($P(\chi^2)$ $(f = 0)$)
- the 5% limit extracted from a fit of the sphericity distributions after the cuts
- the limit determined by the likelihood ratio method

The cuts mentioned in the table correspond to:

- **curr Jet**> 4**GeV:** a current jet candidate with $p_t > 4$GeV
- **Jet,** $Q'^2 > 75$**:** a current jet candidate with $p_t > 4$GeV, $Q'^2 > 75\text{GeV}^2$
- **Jet,** $Q'^2 > 100$**:** a current jet candidate with $p_t > 4$GeV, $Q'^2 > 100\text{GeV}^2$
- **Jet,** $Q'^2 > 75$**,** $n > 5$**:** a current jet candidate with $p_t > 4$GeV, $Q'^2 > 75\text{GeV}^2$, number of tracks in instanton quadrant $n > 5$.
- **2 Jets**> 4**GeV:** two jets with $p_t > 4$GeV
- **Final Cuts:** the final cuts.

The poor description of data by Ariadne in the case of $f = 0$ is probably a result of the higher statistics of the Ariadne sample as compared to the used HERWIG sample. Poor statistics can help to disguise a systematic difference between the two samples, as measured by χ^2.
The likelihood ratio method is an alternative method not suffering from these difficulties.
The limits quoted will be 5.1% for Ariadne and 9.1% for Herwig.

7.5 Limit via cuts

As an independent means of determining a limit on the cross section of instanton-induced events, the number of events passing cuts may be employed.
The ratio of the number of events passing cuts that enlarge the instanton fraction (N_{ins}, see below) and all events passing the offline cuts defined in section 4.3 (N_{offl}) differs for ARIADNE, HERWIG, QCDINS and data. This difference may be used to compute a cross section limit.
The cuts enlarging the instanton fraction chosen are:

- $p_{t,\mathrm{Jet}} > 4\mathrm{GeV}$
- $Q'^2_{rec} > 75\mathrm{GeV}^2$
- number of tracks in instanton quadrant $n > 5$
- sphericity $S > 0.3$
- area cuts in E_t and M as in final cuts.

These are the final cuts with the addition of a sphericity cut.

Generator	$r = N_{\mathrm{ins}}/N_{\mathrm{offl}}$
QCDINS	0.144 ± 0.001
DATA	0.015 ± 0.0003
ARIADNE	0.0162 ± 0.0004
HERWIG	0.0121 ± 0.0005

Table 4: Number of events after instanton enhancing cuts (N_{ins}) over number of events after offline cuts (N_{offl}).

Table 4 shows the ratios $r = N_{\mathrm{ins}}/N_{\mathrm{offl}}$ for the MC generators QCDINS, Ariadne and HERWIG and for data.
The difference $\Delta = r_{\mathrm{Ari}} - r_{\mathrm{Hrw}}$ between Ariadne and Herwig is a measure of the uncertainty of this method. With a value of $\Delta = 0.0162 - 0.0121 = 0.0041$, this difference is significantly larger than the statistical errors, which will be neglected in the following.
The required fraction f of instanton events to be added to the Ariadne Monte Carlo in order to describe the data is calculated by solving the following equation for f:

$$(1 - f) \cdot r_{\mathrm{Ari}} + f \cdot r_{\mathrm{Ins}} = r_{\mathrm{Data}}$$

where the indices Ari, Ins and Data denote the ratios r for Ariadne, QCDINS and data respectively.
To estimate the limiting fraction at 5% confidence f_{lim}, twice the difference Δ between Ariadne and Herwig is added to r_{Data}:

$$(1 - f_{\mathrm{lim}}) \cdot r_{\mathrm{Ari}} + f_{\mathrm{lim}} \cdot r_{\mathrm{Ins}} = r_{\mathrm{Data}} + 2 \cdot \Delta$$

Solving this equation for f_{lim} yields:

$$f_{\mathrm{lim,Ari}} = 0.055$$

for Ariadne and

$$f_{\mathrm{lim,Hrw}} = 0.084$$

for Herwig.

7.6 Theoretical prediction

In order to compare the determined limits with the theoretical predictions, the expected fraction of QCD-instanton induced events has to be determined.

A sample of 213.391 events was generated with QCDINS, with a cross section of σ_{Gen} =182.9pb in a kinematic region larger than that of the final cuts ($Q^2 > 50GeV^2$, $x > 10^{-3}$, $Q'^2 > 64GeV^2$, $x' > 0.35$). After applying the final cuts, 7.942 events remained. This corresponds to a cross section σ_I in the kinematic region determined by the final cuts:

$$\sigma_I = \frac{\#\text{events after final cuts}}{\#\text{eventsgenerated}} \cdot \sigma_{\mathrm{Gen}} = 6.8\mathrm{pb}$$

In the kinematic region determined by the final cuts, the total cross section of the data is $\sigma_{\mathrm{tot}} = 109.6$pb. This is derived from the luminosity $\mathcal{L} = 26\mathrm{pb}^{-1}$ and the number of events N_{offl} passing the final cuts by $\sigma_{\mathrm{tot}} = N_{\mathrm{offl}}/\mathcal{L}$.

This corresponds to an expected fraction of instanton induced events f_I of:

$$f_I = \frac{6.8\mathrm{pb}}{109.6\mathrm{pb}} = 0.062$$

which is about equal to the limits set by the sphericity fit after the final cuts.

8 Systematic errors

8.1 Cut in p_t, Q'^2

To determine the systematic errors on the computed limits, the cuts imposed on the current jet candidate and on the reconstructed Q'^2 have been varied.

The nominal cut values were at $p_{t,\mathrm{Jet}} > 4\mathrm{GeV}$ and $Q'^2 > 75\mathrm{GeV}^2$. The variations were $p_{t,\mathrm{Jet}} > 3\mathrm{GeV}$, $p_{t,\mathrm{Jet}} > 5\mathrm{GeV}$, $Q'^2 > 65\mathrm{GeV}^2$ and $Q'^2 > 85\mathrm{GeV}^2$.

Monte Carlo	$p_t > 3\mathrm{GeV}$	$p_t > 5\mathrm{GeV}$	$Q'^2 > 65\mathrm{GeV}^2$	$Q'^2 > 85\mathrm{GeV}^2$
Herwig	-7%	+32%	-2%	-4%
Ariadne	-13%	+61%	-2%	-4%

Table 5: Systematic errors for the fit method. Shown is the change in per cent of the limit for each possible variation of the cut parameters.

The results for the fit method are shown in table 5. For the different cut variations, the change of the limit is shown in per cent, for the two normal DIS models. The change of the cut on the transverse momentum of the jet dominates the systematic error.

Adding the positive deviations in quadrature, which corresponds to considering only the jet p_t cut variation, and adding them to the limits, we obtain new limits,

$$f_{\mathrm{lim,Ari}} = 0.082$$

for Ariadne and

$$f_{\mathrm{lim,Hrw}} = 0.12$$

for Herwig. These limits have to be compared to the predicted fraction at final cut level of $f = 0.062$.

For the Cuts method, the same studies have been done for Herwig. The result is shown in fig. 6

Monte Carlo	$p_t > 3\mathrm{GeV}$	$p_t > 5\mathrm{GeV}$	$Q'^2 > 65\mathrm{GeV}^2$	$Q'^2 > 85\mathrm{GeV}^2$
Herwig	3%	20%	3%	14%

Table 6: Systematic errors for the cut method. Shown is the change in per cent of the limit for each possible variation of the cut parameters.

Again, the jet p_t cut dominates the error. Adding the positive deviations to the limit yields a limiting fraction of:

$$f_{\mathrm{lim,Hrw,cut}} = 0.10$$

These limits have to be compared to the predicted fraction at offline cut level of $f = 0.006$.

Due to the large uncertainty from the jet cut, other sources of errors like dependencies on energy scales have been neglected.

8.2 Cut in x'

An explicit cut in x' has not been done, because x' cannot be reconstructed well enough. However, such a cut is implied by the final cuts. To see whether this effective cut agrees with the cut of $x' > 0.35$ produced at event generation, a value for x' has been reconstructed in the data and MC. x' is calculated in the following way:

$$x'_{\mathrm{rec}} = \frac{Q'^2_{\mathrm{rec}}}{\hat{s}_{\mathrm{rec}} + Q^2_{\mathrm{DA}} - 2\xi_{\mathrm{rec}} \cdot (p_p p_{\mathrm{Jet}})}$$

where $\hat{s}_{\mathrm{rec}}$ is the square of the center of mass energy of the zufos belonging to the final state, including the jet, ξ_{rec} is the reconstructed momentum fraction of the gluon with respect to the proton, p_p is the four momentum of the proton and p_{Jet} is the four momentum of the jet. ξ_{rec} has been obtained by the formula shown in fig. 10.

Fig 34a) shows the generated x' of the instanton Monte Carlo (solid line) and the reconstructed x'_{rec} (dashed line). The cutoff $x' > 0.35$ is clearly visible. The distribution is considerably smeared due to the reconstruction resolution of x'.

To study the behaviour of the different Monte Carlos and data at x' values below the cutoff of 0.35, the respective distributions have been plotted in fig. 34b): data (bullets), Ariadne (solid), Herwig (dotted) and QCDINS (dashed). The distributions have been normalized to the contents of first four bins, with x' below the cut-off.

In this figure, the different distributions show the same behaviour at low x' values, suggesting that the turn on ofthe x' distribution is modeled correctly, although the resolution of x' will have to be improved to strengthen this claim.

The effect of an x' cut on the final cuts been studied.

Table 7 shows the limiting fractions of instanton induced events determined with Ariadne and Herwig for the final cuts and for the final cuts with the addition of an $x' > 0.35$ cut. The numbers in brackets are the predictions by the instanton MC.

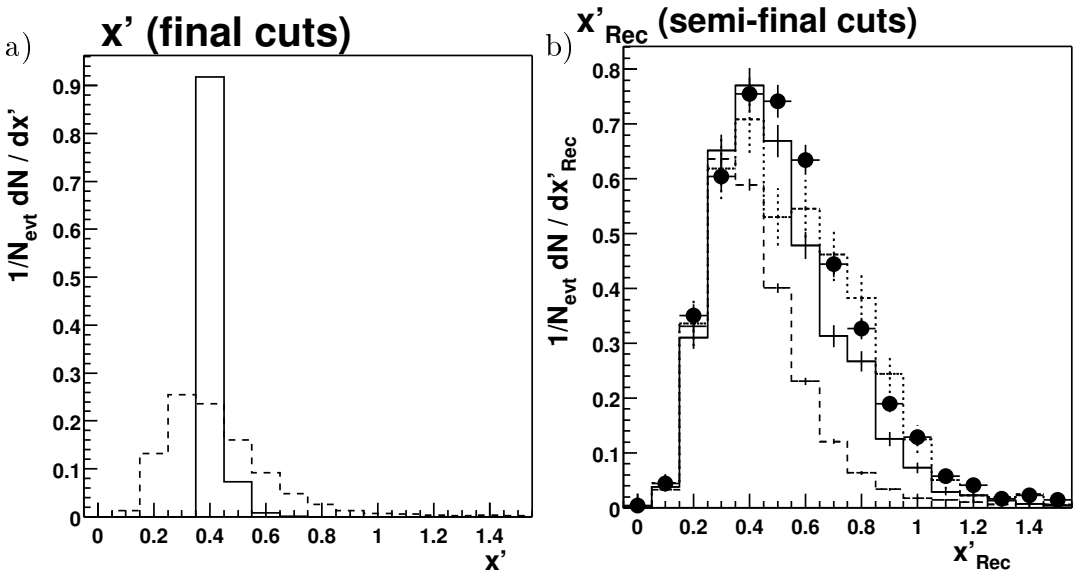

Figure 34:
a) x' generated (solid line) and $x'_{\rm rec}$ reconstructed (dashed line).
b) x' distributions for data (bullets), Ariadne (solid), Herwig (dotted) and QCDINS (dashed). The distributions have been normalized to the contents of the first four bins (x' below cut-off) to study the behaviour below the cutoff value of 0.35.

	Cuts	
Monte Carlo	Final only (predicted)	Final + x' (pred. for final + x')
Ariadne	5.1%(6.2%)	6.4%(6%)
Herwig	9.1%(6.2%)	12%(6%)

Table 7: Introduction of the cut $x'_{\rm rec} > 0.35$. The limits for the Ariadne and Herwig MC are compared limits as in tab. 3 for the final cuts and for the final cuts with an additional x' cut. Theoretical predictions are in brackets.

For both Monte Carlos, the limits with an explicit x' cut are worse by about 30% compared to the limits without that cut.

The limits without the additional x' cut will be quoted as the result, because the reconstruction of x' is not reliable enough to allow a firm conclusion.

All these values have been computed unter the assumption that QCDINS 1.60.1 describes instanton production correctly. In the meantime, QCDINS 2.0 has been released, which could, however, not be included in this analysis. Its use will possibly lead to slightly different results.

9 Conclusion

A limit on the QCD instanton induced cross section has been determined using the data recorded by the ZEUS detector during the year 1997, with a total integrated luminosity of 26pb^{-1}. Deep inelastic scattering events were selected, requiring $Q^2 > 75\text{GeV}^2$ and $x > 10^{-3}$.

Cuts to enrich the instanton fraction (final cuts) have been devised: They are the jet transverse momentum, the reconstructed Q'^2, the transverse energy, the mass and the multiplicity of the instanton candidate. The best strategy to determine a limit on the instanton content of the events after the final cuts has turned out to be a fit to the sphericity distributions.

The upper limit at 95% confidence level of the fraction of instanton events in the DIS sample, including systematic errors, is

$$f_{\text{lim,Hrw}} = 12\%$$

for the Herwig Monte Carlo program.

Using the Ariadne Monte Carlo program yields a limit of

$$f_{\text{lim,Ari}} = 8.2\%.$$

These limits have to be compared to the value predicted by theory (QCDINS 1.6) of:

$$f = 6.2\%$$

An analysis using the new version 2.0 might possibly lead to slightly different results, but could not be performed in the scope of this thesis.

A second, independent, method relying on the best strategy of cuts was not as sensitive and gave weaker limits.

References

[A+83] B. Andersson et al., *Phys. Rep.* **97** (1983) 31.

[ACS95] H. Abramowicz, A. Caldwell and R. Sinkus, *Neural Network based electron identification in the ZEUS Calorimeter*, DESY 95-054, 1995.

[BEK91] S. Bentvelson, J. Engelen and P. Kooijman, "Reconstruction of (x, q^2) and extraction of structure functions in neutral current scattering at hera", in *Physics at HERA*, vol. 1, 23–41, DESY, 1991.

[Bra74] S. Brandt, *Datenanalyse*, Wissenschaftsverlag, 2 ed., 1974.

[Bri98] G. Briskin, *Diffractive Dissociation in ep Deep Inelastic Scattering*, PhD thesis, Tel Aviv University, June 1998.

[C+93] S. Catani et al., "Longitudinally-invariant $k_\perp$-clustering algorithms for hadron-hadron collisions", *Nuclear Physics B* **406** (1993) 187–224, WWW: `http://surya11.cern.ch/users/seymour/ktclus/`.

[CGRS99a] T. Carli, J. Gerigk, A. Ringwald and F. Schrempp, "QCD Instanton-induced Processes in Deep-inelastic Scattering - Search Strategies and Model Dependencies", in *Monte Carlo Generators for HERA Physics*, A. T. Doyle, G. Grindhammer, G. Ingelman and H. Jung, eds., 329–346, 1999, DESY-PROC-1999-02, ISSN 1435-8077.

[CGRS99b] T. Carli, J. Gerigk, A. Ringwald and F. Schrempp, *QCD Instanton-Induced Processes in Deep-Inelastic Scattering - Search Strategies and Model Dependencies*, DESY 99-067, 1999.

[CK97] T. Carli and M. Kuhlen, *Bounds on QCD Instantons from HERA*, DESY 97-151, 1997.

[Dep94] O. Deppe, *Messung des hadronischen Energieflusses in der tiefunelastischen e-p-Streuung*, Diplomarbeit, Universität Hamburg, 1994.

[dJ92] P. de Jong, "Status of the uranium calorimeter reconstruction software", *ZEUS-Note 92-019* (1992).

[dK94] M. de Kamps, "Changes and extensions of the calorimeter reconstruction programme", *ZEUS-Note 94-014* (1994).

[Dor91] W. Dorth, *LAZE, Logical Access to ZEUS Events*, ZEUS-Note 91-069, 1991.

[Ell98] J. Ellis, *The Standard Model of Particle Physics*, CERN-TH/98-403, 1998.

[Ger98] J. Gerigk, *QCD-Instanton-induzierte Prozesse in tiefunelastischer $e^{\pm}p$-Streuung*, Diplomarbeit, Universität Hamburg, Hamburg, November 1998.

[GRS95a] M. Gibbs, A. Ringwald and F. Schrempp, in *Quarks '94*, D. Grigoriev, V. Matveev, V. Rubakov, D. Son and A. Tavkhelidze, eds., p. 170, World Scientific, Singapore, 1995, hep-ph/9411217.

[GRS95b] M. Gibbs, A. Ringwald and F. Schrempp, *QCD-Instanton Induced Final States in Deep Inelastic Scattering*, DESY 95-119, 1995.

[GRS95c] M. Gibbs, A. Ringwald and F. Schrempp, "QCD-Instanton Induced Final States in Deep Inelastic Scattering", in *Workshop on deep inelastic scattering and QCD*, J.-F. Laporte and Y. Sirois, eds., 341–344, Paris, April 1995, hep-ph/9506392.

[H1 96a] H1 Collaboration, *Nucl. Phys.* **B480** (1996) 3.

[H1 96b] H1 Collaboration, *Z. Phys* **C72** (1996) 573.

[HWMN+99] R. Hall-Wilton, N. McCubbin, P. Nylander et al., *The CTD tracking resolution*, ZEUS-Note 99-027, 1999.

[IER97] G. Ingelman, A. Edin and J. Rathsman, *Comp. Phys. Commun.* **101** (1997) 108.

[Kuh97] M. Kuhlen, *QCD and the Hadronic Final State in Deep Inelastic Scattering at HERA*, Habilitationsschrift, December 1997.

[Lön92] L. Lönnblad, *Comp. Phys. Commun.* **71** (1992) 15.

[M+92] G. Marchesini et al., *Comp. Phys. Commun.* **67** (1992) 465.

[Mik00] S. Mikocki, Proceeding of DIS2000 conference, April 2000, http://hep.ph.liv.ac.uk/DIS2000/DIS2000_proceedings.html.

[MRS97a] S. Moch, A. Ringwald and F. Schrempp, in *Deep Inelastic Scattering and QCD (DIS 97)*, J. Repond and D. Krakauer, eds., p. 1007, American Institute of Physics, Woodbury, New York, 1997, hep-ph/9706400.

[MRS97b] S. Moch, A. Ringwald and F. Schrempp, "Instantons in deep-inelastic scattering: The simplest process", *Nucl. Phys.* **B 507** (1997) 134–156.

[Ohr96] K. Ohrenberg, *Measurement of the Proton Structure Funkction F_2 Using the Hadron Electron Separator of the ZEUS Detector at HERA*, PhD thesis, Universität Hamburg, 1996, DESY-F35D-96-17.

[Okr99] J. R. Okrasiński, *Measurements of the Hadronic Final State in Deep Inelastic Scattering at HERA*, PhD thesis, Pennsylvania State University, August 1999, ISSN 1435-8085, DESY-THESIS-1999-018.

[RS94] A. Ringwald and F. Schrempp, *Towards the Phenomenology of QCD-Instanton Induced Particle Production at HERA*, DESY 94-197, 1994.

[RS98a] A. Ringwald and F. Schrempp, *Confronting Instanton Perturbation Theory with QCD Lattice Results*, hep-lat/9903039, DESY 98-201, 1998.

[RS98b] A. Ringwald and F. Schrempp, "Instanton-induced cross-sections in deep-inelastic scattering", *Phys. Lett.* **B 438** (1998) 217–228.

[Sjö94] T. Sjöstrand, *Comp. Phys. Commun.* **82** (1994) 74.

[Spi93a] H. Spiesberger, "Django 6 version 2.4.", *unpublished program manual* (1993).

[Spi93b] H. Spiesberger, "Heracles version 4.5.2", *unpublished program manual* (1993).

[ST98] D. A. Smith and M. J. Teper, "Topological structure of the SU(3) vacuum", *Physical Review D* **58** (1998) 014505.

[tH76a] G. 't Hooft, *Phys. Rev. Lett.* **37** (1976) 8.

[tH76b] G. 't Hooft, *Phys. Rev.* **D 14** (1976) 3432.

[tH78] G. 't Hooft, *Phys. Rev.* **D 18** (1978) 2199, (Erratum).

[tH86] G. 't Hooft, *Phys. Rep.* **142** (1986) 357.

[WZ79] S. L. Wu and G. Zobernig, "A Method of Three-Jet Analysis in e^+e^- Annihilation", *Z. Physik C, Particles and Fields* **2** (1979) 107–110.

[ZEU92] ZEUS Collaboration, *A Measurement of* $\sigma_{tot}(\gamma p)$ *at* $\sqrt{s}$ *=210 GeV*, DESY 92-127, 1992.

[ZEU93] ZEUS Collaboration, *The ZEUS Detector, Status Report 1993*, DESY, 1993.

List of Figures

1 Double-Well Potential . . . 7
2 Degenerate Vaccum . . . 9
3 The process diagram of an instanton induced DIS process (adapted from [Kuh97]) . . . 11
4 The calorimeter. Inside this (not shown) are tracking chambers. . . . 13
5 FCAL and RCAL . . . 14
6 Trigger and DAQ . . . 16
7 Sample event . . . 18
8 Schematic of the PC farm . . . 19
9 Reconstruction file states . . . 21
10 Instanon kinematic variables . . . 23
11 Jet p_t vs Current Quark p_t . . . 30
12 Q'^2 resolution, DA method with small jet . . . 33
13 Comparison Data and Monte Carlo - kinematic variables . . . 35
14 Comparison of Data and Monte Carlo: $E - P_z$, $E_{t,\mathrm{tot}}$ . . . 36
15 Comparison of Data and Monte Carlo: E and p_t of current jet candidate. . . . 37
16 Comparison of Data and Monte Carlo: E_t, n_{tracks} . . . 39
17 Comparison of Q'^2_{rec} . . . 40
18 Jet multiplicity comparison . . . 41
19 Division in two quadrants . . . 43
20 Sphericity resolution . . . 44
21 Sphericity distribution (hadron vs detector) . . . 45
22 Comparison Data and Monte Carlo: Sphericity 2 . . . 47
23 M vs S . . . 49
24 Correlations of E_t/M, E_t/E . . . 50
25 Et Vs M, ratio NDIS/QCDINS . . . 51
26 comparison QCDINS normal and low x', Q' . . . 52
27 comparison jet p_t QCDINS normal and low x', Q' . . . 53
28 comparison of x' for normal/low parameter QCDINS . . . 54
29 Comparison of Q'^2_{rec} (final cuts) . . . 56
30 Weights from Sphericity distributions . . . 57
31 Result of Weighting . . . 58
32 Result of Weighting . . . 59
33 χ^2 vs fraction f . . . 59
34 x' reconstruction . . . 67